People's Democratic Republic of Algeria

Ministry of Higher Education and Scientific Research

University M'Hamed BOUGARA- Boumerdes

Institute of Electrical and Electronic

Engineering Department of Power and Control

Engineering

Project Report Presented in Partial Fulfilment of

the Requirements of the Degree of

'MASTER'

In Electrical and Electronic engineering

Option: Power Engineering

Title:

Sizing of PV Pumping System with Optimizing MPPT Algorithm

Presented By:

- **Malik BENMBAREK**
- **Mouhaned DAIF**

Supervisor:

Pr. KHELDOUN. A

Co-Supervisor:

Dr. Khettab Soufian

June 2024

Dedication

To my beloved parents
To my sister and brothers
To my dear aunt B.Z and my grandmother
To all my friends ISRRCYM

Thank you for your everlasting
love and warm encouragement throughout my academic career.

Mouhaned

To my dear father
To my lovely mother
To my siblings
To my friends
Thank you all for what you have
done for me. much love.

Malik

Acknowledgements

First and foremost, Our deepest thanks are to ALLAH, the most gracious most merciful for blessing us with strength and guidance throughout this journey into the delivery of this modest work.

I am sincerely thankful to my beloved parents, siblings, and friends whose encouragement, support, love, and unwavering dedication to my education have been invaluable. I am truly grateful for their presence in my life.

We would like to express our deep-felt gratitude to our supervisor Pr. A.KHELDOUN for his wisdom, guidance, and support.

Lastly, I extend my heartfelt thanks to all those individuals who have directly or indirectly assisted me in the successful completion of this project including our Co-Supervisor Dr. Khettab Soufian, also we would like to express our special thanks to Dr. Hamza Ouazene, Dr. Bilal Taghezouit, Dr. Walid Merrouche, Dr. Yahia Bakelli, Dr. Houria Assem, Dr. Hadil Diaf, Dr. Hamza Belmadani.

Abstract

This report covers a comprehensive study of the sizing, modeling and simulation of a stand-alone solar water pumping system in El Oued, Algeria. The initial part involves selecting a farm located in Hassi Khalifa, El Oued, Algeria, which has an average water consumption of 4 m^3/h. The irrigated site covers 1 hectare (10,000 square meters) of land. Sizing such a system has been carried out using different tools such as Cropwat, Climwat, and PVgis. Sizing has led to the selection of a 2.2 kW submersible pump, 3.19 kW PV array, 3 kW inverter, and a 74 m^2 Tank of height 3 m. System dynamic modeling is done using MATLAB/Simulink which contains several models of sub-systems such as solar arrays, DC-DC boost converter, two-level inverter, Squirrel cage IM, and centrifugal pump, This dynamic modeling has been developed based on the sizing of the system. To improve further the overall system's efficiency, an enhanced P&O MPPT algorithm has been developed. Moreover, a DTC algorithm is used to regulate both the motor's speed and torque. Various numerical simulations were conducted to illustrate and validate the effectiveness of this system. MATLAB/Simulink simulation shows that this system can deliver the required energy needed for the farm to satisfy all the requirements.

Keywords: Induction Motor (IM); Perturbation and Observation (P&O); Maximum Power Point Tracking (MPPT); Direct Torque Control (DTC)

Contents

List of Figures

List of Tables

List of Abbreviations

AC Alternating Current

BLDC Brushless DC Electric Motor

DC Direct Current

DTC Direct Torque Control

EMI Electromagnetic Induction

FOC Field Oriented Control

Id Magnetizing current

IFOC Indirect Field-Oriented Control

IM Induction Motors

Iq Torque-producing current

MPPT Maximum Power Point Tracking

PO Perturb and Observe

PSH Peak Sun Hour

PV Photovoltaic

PVG Photovoltaic Generator

PWM Pulse Width Modulation

SWPS Solar Water Pumping Systems

SynRM Synchronous Reluctance Motor

v/f Voltage-frequency

VS Variable Speed

General Introduction

For over a century and a half, fossil fuels—comprising coal, oil, and natural gas—have served as the backbone of global economies, presently accounting for approximately 80% of the world's energy consumption **?**. As a result, fossil generation is responsible for about 40 % of the global CO2 from greenhouse gases, and this is estimated to be increasing due to economic and population growth, which may drive up the energy demand **?**. That is why seeking alternative sources of energy for reducing carbon dioxide emissions and ensuring secure, clean and affordable energy is crucial.

"Solar Energy" then is one of the greatest alternative sources, a solution for achieving more sustainable energy systems, and that is because of its renewability, less Environmental Impact, Cost-Effectiveness, minimal maintenance, Energy Independence and Security **?**.

One of the applications of Solar Energy is a photovoltaic generator (PVG), which involves converting light energy into electrical energy through the photovoltaic effect. When sunlight strikes a solar cell, made primarily of semiconductor materials like silicon, it energizes electrons within the material. These energized electrons flow as an electrical current which can then be harnessed to power electrical devices or systems **?**

In Algeria, stand-alone water pumping systems powered by photovoltaic energy are the most common application, especially in remote areas where accessing the grid is a bit challenging. These solar-powered systems are mainly used for providing potable water and supporting agricultural activities. Significant research has been conducted to evaluate the efficiency of solar water pumping systems (SWPS) across various nations situated in tropical zones, where conditions are highly favorable for their use.

In the arid landscapes of El Oued, Algeria, water management is crucial for sustainable agriculture. This thesis investigates the implementation of renewable energy solutions for agricultural irrigation by designing, modeling, and simulating a stand-alone solar water pumping system suitable for a farm in Hassi Khalifa, a region characterized by its reliance on agriculture as a primary source of income. The selected farm, covering a hectare of land dedicated to potato cultivation, faces significant challenges due to its water needs—approximately 4 cubic meters per hour—necessitating an efficient and sustainable approach to water extraction and distribution.

The design process began with a detailed analysis of the site's geographical and climatic conditions, utilizing tools such as Cropwat for crop water requirements and Climwat for climate data analysis, alongside PVgis for assessing solar radiation availability. These tools were integral in determining the optimal size of the solar photovoltaic (PV) array and associated components needed to meet the farm's water requirements effectively. Furthermore,

the economic feasibility of the system was analyzed using Homer software, ensuring that the proposed solution is not only technically viable but also economically advantageous.

Central to this study is the use of MATLAB/Simulink for dynamic modeling of the system. This includes comprehensive simulations of the solar arrays, DC-DC boost converter, two-level inverter, and the integration of a squirrel cage induction motor with a centrifugal pump, all tailored to the specifics of the farm's requirements. A key innovation in this system is the incorporation of a Perturb and Observe (P&O) algorithm-based Maximum Power Point Tracking (MPPT) to optimize the energy harvested from the PV array. Additionally, a Direct Torque Control (DTC) algorithm enhances the control over the motor's speed and torque, further improving the system's efficiency.

The report is structured into four chapters as follows:

- The first chapter aims to provide a literature review on some of the current technologies and advancements in solar pumping systems.
- The second chapter covers the solar water pumping system sizing.
- The third chapter focuses on the system's modeling.
- The last and fourth chapter will cover the simulation's results and discussion.

Chapter 1

Literature Review

Introduction

Global demand for water is projected to increase from 20% up to 25% by 2050, driven by various factors such as population growth, economic development, climate change, and extensive water consumption patterns **?**, water resource then comes as an essential need to satisfy different human demands, ensures food and health sustainability and promotes social and economic progress. Moreover, though there has been a remarkable increase in the share of drinking water, as in Algeria a study in **?** shows that the share of drinking water has increased from 16% in 1975 to 36% in 2019. However, agriculture remains the largest consumer of water, accounting for around 70% of all water withdrawals**?**. This percentage will only increase due to some severe risks posed by water shortages that may threaten food security**?**. As a result, supplying water has become a necessity nowadays, with lower financial and environmental costs more regions will benefit from it, especially Water supplies for household use, livestock, and irrigation in isolated areas. Water Pumping is the best solution for these rural areas which mainly depend on underground water resources that can be exploited for different daily usage for instance irrigation.

Water pumping applications depend on different power sources, some are widely used such as electric or diesel-powered pumps, but these types of sources still have many issues as for diesel generators they are used in remote areas and villages mostly, these engines require regular maintenance and high running cost, also they contribute to environmental pollution, either through the emissions from the combustion process or due to oil leakage into water sources **?**. Additionally, it may be a bit challenging for fuel transportation as these rural regions are far from fuel distribution centers. Now for systems based on electricity from a grid connection, this seems hard to implement, especially for rural areas where many parameters are included such as The length of the line, the type of terrain, and the required capacity of the transformer. For instance, longer distances require thicker wiring and potentially additional

transformers to manage voltage drop, which can significantly increase costs**?**. Photovoltaic pumping is one of the most promising applications of solar energy; the technology is similar to any other conventional water pumping system except that the power source is solar energy**?**.

Solar water pumping minimizes the dependence on diesel, gas, or coal-based electricity. As pumping systems based on PV energy offer several advantages over diesel or traditional electric systems, particularly in terms of cost-effectiveness, environmental impact, and applicability in remote locations**??**.

PV water pumping has become increasingly significant in recent years, This growth is driven not only by technological advancements and decreasing costs but also by the sustainability and reliability that PV systems offer, especially in regions without stable electricity access or where diesel fuel is expensive and logistically challenging to supply. Furthermore, the trend towards solar PV is not just a matter of energy generation but also environmental consideration, as these systems produce no direct emissions and are typically quieter and cleaner compared to traditional diesel pumps. According to the International Energy Agency's forecast in 2010, the solar PV market was expected to see an average annual growth rate of 17% over the following decade, which would lead to a substantial increase in global cumulative installed PV power capacity—reaching 200 GW by 2020 and an impressive 3000 GW by 2040 **?**.

A stand-alone photovoltaic system is a solar energy system that is not connected to an electrical grid. It is used for the production of electricity on-site and can be installed anywhere. Stand-alone systems are typically smaller than grid-connected PV systems and have lower installation costs, since they do not require additional infrastructure and their installation does not place additional load on the grid, although they require a high initial investment but with the appropriate study it can be profitable by the time.

This chapter provides a general overview of solar pumping systems, some of the recent research in the field, and some statistical analysis of its use globally and domestically.

1.1 Configuration and classification of SWPS

Stand-alone water pumping systems are known for their simplicity, as they are independent of grid connection. They are mainly based on PV technology that converts sunlight into electricity to drive a pump. These PV panels are connected in series and parallel to form arrays, which with the help of other components help drive a motor (DC or AC) that converts electrical energy to a hydraulic one which shows in the form of a flow rate in the output of the pump. Stand-alone SWPS generally consists of the following components:

- PV array,
- Pump controller,
- Charge controller,
- inverter,
- Batteries,
- Tank storage,
- Motor-pump system.

The various classifications of Solar Water Pumping Systems (SWPS) are determined based on which component the different topologies are built from, this will be outlined in the following sub-sections.

1.1.1 SWPS based on energy storage

There are two types of storage systems; energy storage in batteries and water storage in large tank. As PV panel does not work at night and the efficiency becomes lesser during cloudy weather, the storage system is designed as a one- or two-day back-up**?** in order to ensure system consistency. Battery architecture systems are simpler as in general they require fewer components compared to tank architecture, as **?** showed from a techno-economic analysis carried out in the rural village of Gogma, Burkina Faso that the initial and life cycle costs for a PVWPS based on batteries are lesser than a one based on tanks. However, as batteries must be replaced regularly and recycled adequately, PVWPS' financial accessibility could increase, and it could get even worse if lead-acid batteries are used as they on average last at most four years -on harsh Saharan climatic conditions-, making their replacements unavoidable**?**.
Tank architecture then comes as the best solution, especially for rural areas, since it lasts the whole PVWPS lifetime and won't require any further maintenance. figure 1.1 below shows a comparison between both architectures.

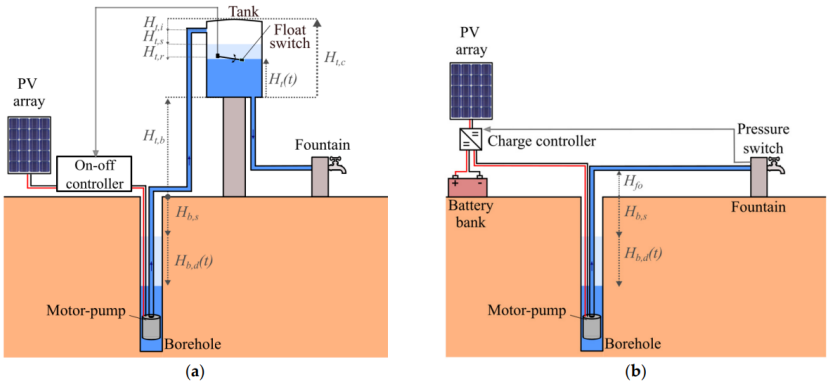

FIGURE 1.1: Different PVWPS Architectures: a) Tank based, b) Battery based

1.1.2 SWPS based on the type of motor

The electrical machines are an important part of the photovoltaic pumping systems. Electrical machines are devices that convert electrical energy into the mechanical energy of a rotating shaft. Two primary types of motors are utilized in photovoltaic pumping systems: induction motors (IM) and direct current motors (DC). The classification of these motors is shown in Figure 1.2 **?**.

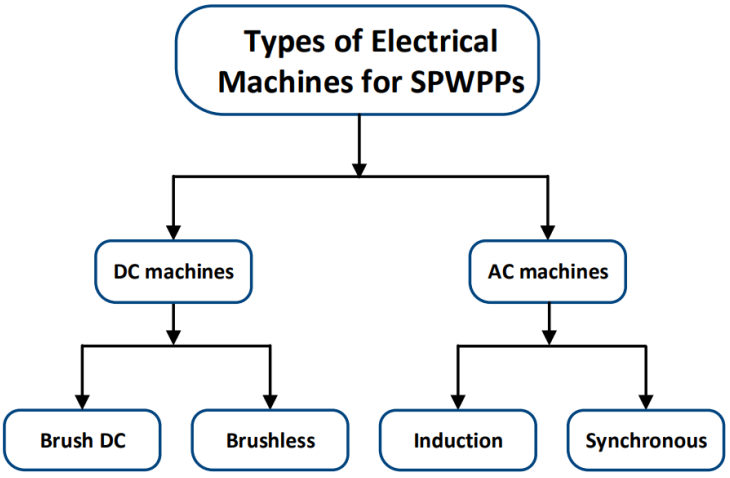

FIGURE 1.2: Main types of electrical machines for photovoltaic pump applications.

DC machines are mainly used for low-power applications, where there are no complicated power converters needed because it is possible in some cases to connect it directly to the PV array. in **?** The author describes one of the earliest studies on using DC motors for water pumping applications. However, these DC machines are expensive, less reliable, and require more maintenance, especially when used in high-power applications. Along with the direct current machines, induction machines with squirrel cage rotors are among the most

technologically advanced machines; they provide more power and more efficiency than DC machines **?**, also they provide a wide speed range. Though it may seem that induction motors are more adequate for solar water pumping applications, still The appropriate electrical machine should be chosen depending on the system's size, cost, power input, availability, and maintenance status **?**. Tables 1.1 and 1.2 below present Some of the advantages and disadvantages of both types of electrical machines.

TABLE 1.1: Advantages and Disadvantages of DC machines

Advantages	**Disadvantages**
Can be connected directly without a special control or by DC-DC	Needs maintenance because of low brush life
High initial torque on the shaft	Cogging at low rotational speeds
Easy speed control (for brushed)	Power losses due to commutator
A broad range of speed controls	Sparks can cause EMI
Fast reaction to the load variation	Risk of commutation failure
Suitable for pumping due to their speed-torque characteristics	Can be damaged in humid environment

TABLE 1.2: Advantages and Disadvantages of AC machines

Advantages	**Disadvantages**
Low cost	Low starting torque value
Robust construction	High startup current
Availability for wide power range	Expensive control system
Relatively high power factor	Efficiency drops at low loads
Does not require frequent maintenance	Does not operate well at speeds less than 30% of its nominal

The literature discusses different potential topologies on solar water pumping systems, including both AC and DC machines. a pumping system based on an induction motor for processing the water from a well in the desert is proposed in [31], where a mathematical

model of the induction motor was built based on Thevenin's theorem. A model enables the representation of the flow rate and system efficiency in relation to the supply frequency and pumping head as well as the motor torque in relation to speed at various supply frequencies. In [32] the authors propose a method for optimizing the operation of a photovoltaic pumping system that uses an induction motor. The optimization variable is the quantity of pumped water and to achieve the maximum daily output the efficiency of the motor-driven system is optimized at each operating point.

So as seen, there is too much research going in which type of motors is better to be used for SWPS, in terms of cost-effectiveness and reliability, and this could even include other types of motors such as BLDC or SynRM.

1.1.3 SWPS based on the type of pump

Pumps are of different types, and hence many SWPS based on pump topologies are found in the literature. The table 1.3 below shows the available types of pumps for different applications in SWPS.

TABLE 1.3: Types of pumps and their application

Pump	**Application**
Submersible pumps	Ideal for deep wells where water needs to be lifted to the surface. These pumps are placed underwater and are highly efficient in deep water sources.
Surface pump	Suitable for shallow water sources and typically used for small-scale irrigation or livestock watering. These are installed above the water level and can include booster pumps for increased pressure.

Pumps can generally be categorized into two main types based on their operating principle: dynamic (or kinetic) pumps and positive displacement pumps. more details are shown in the list below:

1. Dynamic Pumps: These pumps impart velocity and pressure to the fluid as it moves through the pump through the action of a rotating impeller. The kinetic energy is then converted into pressure energy in the discharge pipe. Dynamic pumps are subdivided further into centrifugal pumps, which are the most common, and axial flow pumps. They are typically used for large-volume pumping applications with relatively low-pressure increases and are known for their efficiency in continuous flow situations.

2. Positive Displacement Pumps: These pumps move a fixed amount of fluid with each stroke or cycle by trapping a fixed amount of fluid and then displacing it into the discharge pipe. This category includes gear pumps, diaphragm pumps, and piston pumps, among others. Positive displacement pumps are suited for applications requiring high pressures and accurate dosing because they provide a constant flow regardless of the system pressure, making them ideal for viscous fluids or fluids containing suspended solids.

Figure 1.3 below illustrates different SWPS topologies based on the type of pump

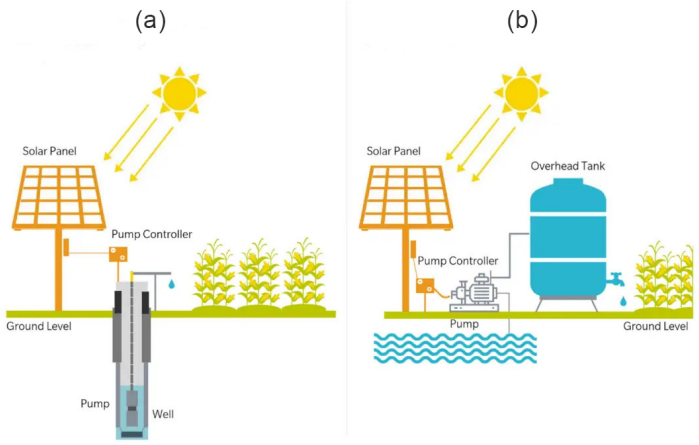

FIGURE 1.3: SWPS based on pump type : (a) Submersible pump, (b) Surface pump

1.1.4 SWPS based on power source:

The configuration of SWPS could vary too based on which type of power source is used to feed the motor-pump system, therefore based on application and usage, they can be classified as stand-alone systems, on-grid solar power systems **?**. Grid-tied systems are designed to operate in parallel with the solar array and it is connected to the electric utility grid. In contrast, Stand-alone systems are designed to operate independently of the electric utility grid and are generally designed and sized to supply certain DC or AC electrical loads [18].

1.1.4.1 Stand-alone configuration:

A stand-alone SWPS system is not connected to any power grid and this refers to its being called an off-grid system, moreover, it relies solely on solar energy from the PV array. This type of system is mainly installed in remote areas where there is no access to the utility grid, which is why They typically include batteries for energy storage to ensure water supply during non-sunny periods **?**. Advantageously, stand-alone solar power owners pay no monthly electricity bills because the equipment completely belongs to them **? ?**, which in terms of cost-effectiveness seems to be beneficial. Stand-alone in return have different installations based on which components are included in the SWPS, and they could be further classified into:**?**

1. Stand-alone solar power system supplying only DC loads,
2. Stand-alone solar power system with an electronic control circuit to extend its duty cycle,
3. Stand-alone solar power system supplying DC loads, electronic control circuit for extending the duty cycle and simultaneously charging the storage battery for power supply at night or whenever there is no sunlight, and
4. Stand-alone solar power system with DC/AC converter, which supplies AC loads, supplies electronic control circuit for duty cycle extension, and simultaneously charging storage battery for emergency supply.

Also the figure 1.4 below shows a typical stand-alone SWPS configuration, so it is well-noticeable that such systems do not require too many components to be included, also there is no need for batteries in irrigation applications where tanks could be a great backup.

1.1.4.2 Hybrid (on-grid) configuration:

These systems are connected to the electrical grid and can use solar power as a primary source but switch to the grid when solar energy is insufficient. They often incorporate inverters to convert DC from the solar panels to alternating current (AC) compatible with the grid. This setup allows for more consistent operation but is generally more complex and costly due to additional components like inverters and grid connection requirements **?**. Figure 1.5 below illustrates a typical on-grid SWPS, we notice that this type of configuration is hybrid meaning that it could use both powers from PV and grid or from PV and a diesel generator, and this is based on the following scenarios:

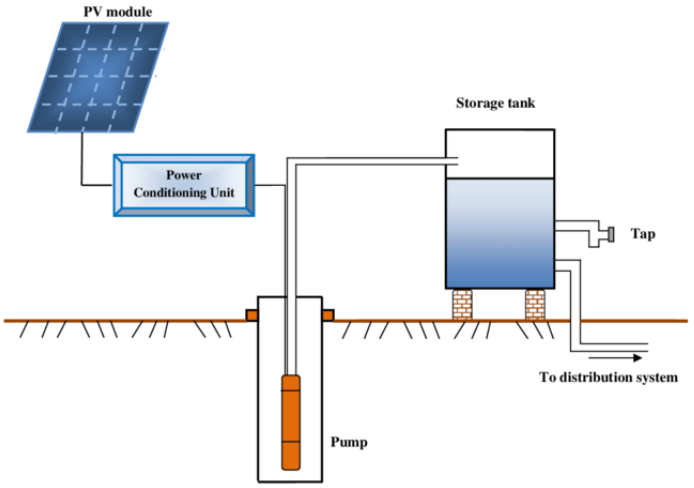

FIGURE 1.4: a typical stand-alone SWPS configuration

a When solar energy is available during the day and there is a need for pumping, the photovoltaic (PV) array powers the pump.

b At night, when there is no solar energy and pumping is still necessary, the system switches to grid power.

c If the solar energy is insufficient to run the pump at full capacity, the grid supplies the necessary additional power.

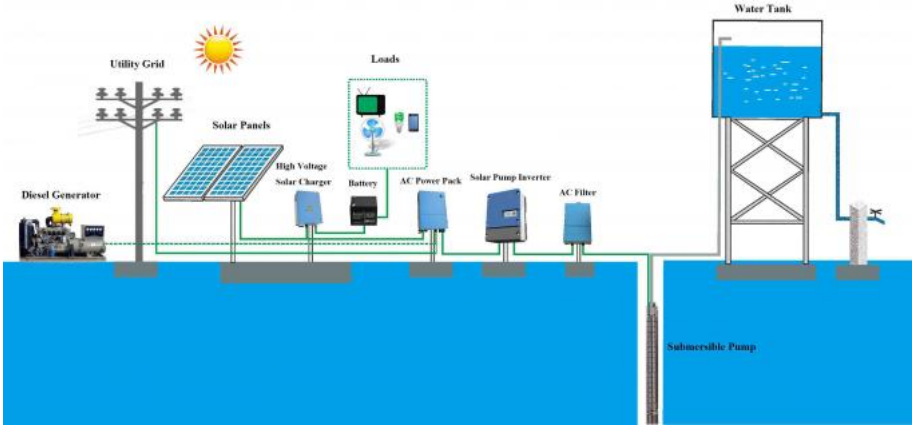

FIGURE 1.5: a typical on-grid SWPS configuration

1.2 Previous work on SWPS:

Much research has been done regarding the construction of SWPS with different components included, each of which contributes to optimizing this system for a more sustainable

water supply, especially in rural areas where water interruptions could do some serious damage. The literature proposed different motors as shown above, and each has its pros and cons as in this paper **?** authors proposed the use of a BLDC motor along with a DC-DC boost converter and a VSI to control the motor. Figure 1.6 shows the proposed system's configuration.

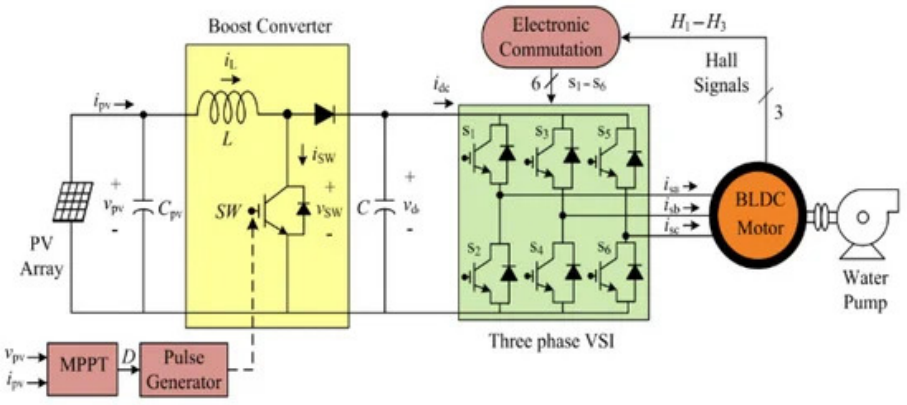

FIGURE 1.6: Configuration of the solar PV boost converter BLDC motor-driven water pump

An MPPT controller was used to control the DC-DC boost switching, as for this research **?** a comparison between the P&O algorithm and cuckoo search algorithm is done. The results show that the P&O algorithm failed to track the global MPP, while the cuckoo search did successfully, under partial shading conditions. Another study in **?** compared three different MPPTs and the results were as follows: The best oscillation in P&O MPPT technique, the best rise time, settling time in Fractional voltage current circuit (open, short) MPPT, and the Incremental conductance MPPT has the best performance in settling time.

The literature also discussed an important aspect of SWPS, as in **?** three solar water pump systems based on their storage configurations are considered for a rural area in Iran, one without any storage, another with battery storage and one that uses water tank as storage, the table 1.4 shows a comparison between these storage configurations.

TABLE 1.4: Compare different storage configurations

Configuration	**Cost (CA$)**	**Advantages**	**Disadvantages**
Without storage	30,000	Low cost	Unreliable
Battery storage	72,800	Provide a constant power to pump, which results in a higher life span of the pump	Replacement and maintenance cost
Water tank storage	56,000	High life-span	Difficulty in build and installation of high-capacity water tanks

The results then show that a system with water tank storage is recommended for the studied area because not only does it guarantee the reliability of the system, but also provides a storage system at a reasonable price.

Several papers have also covered the control strategy of the motor that is important for solar water pumping systems. An appropriate motor control technique might reduce the size of the PV array that is required to reach the specified energy usage, and hence, decrease the overall cost of the photovoltaic pumping system. For IM there are mainly two control techniques that are commonly used in SWPS applications which are: Scalar control and the other one is vector control **?**. In **?** authors proposed the use of direct torque control (DTC) for a developed hybrid control algorithm for pressure maintenance, using a programmable logic controller that operates the DTC-based control system according to the proposed hybrid algorithm. In **?** the authors propose a DTC technique that calculates the vector terminal voltage (VS) module based on the estimated electromagnetic torque value in comparison to the baseline. If the torque approaches its reference value, the VS module steadily drops until it reaches zero. The electromagnetic torque error and stator flux error together determine the angle of the vector VS. Finally, the vector VS is produced using the modulation vector. The use of scalar control would make a more simple control strategy for IM, sometimes it is also known as voltage-frequency (v/f) control. In **?** a novel scalar technique for independent control of the main winding and auxiliary winding of a single-phase induction motor is proposed. A two-inverter topology is proposed and implemented in the voltage–frequency control technique. The proposed method excludes the disadvantages of using a capacitor attached to the auxiliary winding. The technique enhances overall drive performance in terms of energy savings and torque profile throughout the whole speed range. For Field oriented control (FOC), the authors in **?** authors propose Field-Oriented Control (FOC) by adjusting a magnetizing current (Id) and a torque-producing current (Iq) in an equal ratio, to maintain a constant ratio of the currents. below, table 1.5 shows some major results related to the implementation of various electrical drive control techniques for SWPS.

Table 1.5: Application of different drive control methods for SWPS

Control Strategy	**Main Results**
FOC	This study examines a photovoltaic electromechanical system that consists of a PV array, a DC-DC converter with impedance A torque, and the d-q components of stator current remain constant regardless of the insolation intensity variation. **?**
IFOC	The suggested technique relies on indirect field-oriented control (IFOC), ch involvles whi minimizing induction motor losses. The losses are reduced and the efficiency is increased by 12%, and 2.5% under 375 W/m2 and 750W/m2 radiation, respectively. **?**
DTC	Rotor speed estimation of direct torque control (DTC) of an induction motor drive used for solar PV-driven water pumping using a unique robust model reference adaptive system (MRAS) technique is proposed. A method based on second-order generalized integration has been developed to estimate the rotor flux in a stationary domain. **?**

1.3 Conclusion:

In this chapter we had an overview on SWPS, starting from having an introduction about these systems, then discussing the different configurations, and we end it up with a literature review on SWPS.

Chapter 2

Stand-alone PV Water Pumping System Sizing

Introduction

A stand-alone PV water pumping system sizing will be discussed in this chapter, starting from the selection of the studied farm; its geographic location, the climatic conditions in that region, and many different parameters that facilitate the system's sizing. Moreover, many software such as PVgis, Cropwat, and Climwat are used to get the data required to size our water pump. Also, with the use of mathematical equations, we get the required water flow rate [m2/h] and then size the pump based on it. The rest of the system's components are sized accordingly based on the motor-pump system needs.

2.1 The site selection:

Algeria is a big country with 2,381,741 km2 total land, making it the world's tenth largest nation by area, and the largest nation in Africa **?**. 80% of Algeria's land is considered a desert, which means it covers four-fifths of the country's total area, that is what makes Algeria a perfect spot for solar energy applications in Africa. Moreover, Algeria receives approximately 3,000 hours of sunshine per year, creating ideal conditions for solar energy production used in different applications to meet the domestic, agricultural, and industrial water needs of the region. The government has ambitious plans to harness this resource, aiming to achieve 15,000 megawatts of solar energy capacity by 2035 **?**.

The Algerian Sahara is also known for its significant contributions to agriculture and that is by transforming what was once a barren desert into productive agricultural land, knowing

that the agriculture sector contributes on average about 12% of Algeria's GDP and employs at least 20 percent of the population in rural areas **?**.

The region of El Oued specifically, has been transformed into one of Algeria's main agricultural centers, leveraging many of its geographical privileges such as lying on the Albian aquifer (40 – 60 meters deep water reservoirs), a mild and sunny winter climate, abundant sunlight and vast land area, the figure 2.1 shows the Global underground water resources, which reflects on the availability of underground water in the region of Eloued as it falls into the major regional aquifer systems. These previously mentioned factors would help in growing a variety of the most needed crops in Algeria namely; potatoes, tomatoes, onions, and peanuts. These crops are largely grown organically due to the high sunlight which reduces the incidence of plant diseases and diminishes the need for pesticides **?**. Irrigation then is highly needed to produce the right amounts of water required by these crops to be harvested at their specific seasons without any delay, therefore most of the irrigation systems in the region of Eloued are based on pumps (surface or submersible) which are supplied generally from the utility grid or by the use of diesel generators, this may lead to some inconveniences, especially for some rural cities where no access to grid system is available, and fuel transportation may seem a bit challenging, this will just lead to more water shortages. As a result, pumping systems based on solar energy are becoming a trend, especially for irrigation applications in Saharan rural regions **?**, where the metrological conditions are suitable for optimal electricity generation through the use of PV arrays, thus fewer water shortages will occur.

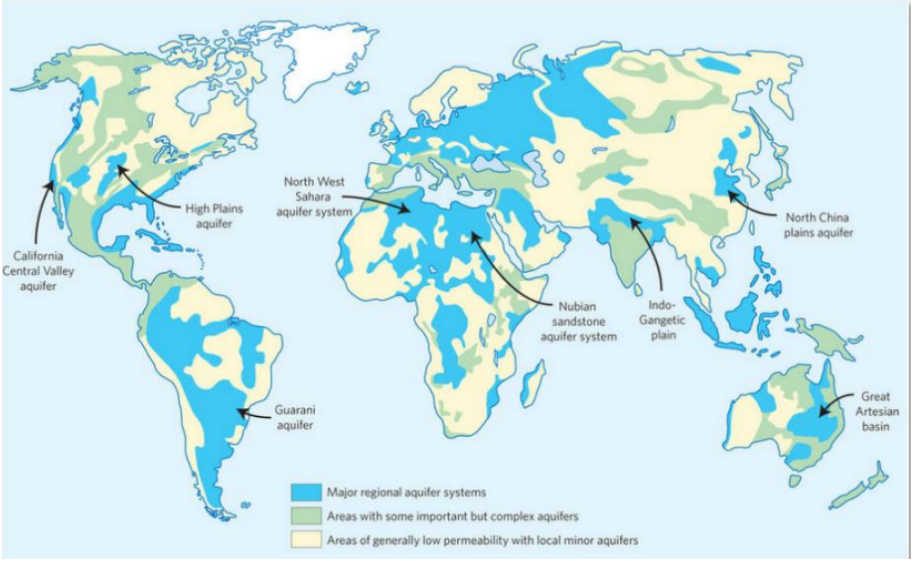

FIGURE 2.1: Global underground water resources

Based on the factors above, a site was selected in Hassi-Khalifa, situated in the region of ELoued between 33° 33 44 north, 6° 59 25 east with 1112 km2 of total area **?**, this region is 20km away from ELoued **?**, The figure 2.2 below shows its geographical position.

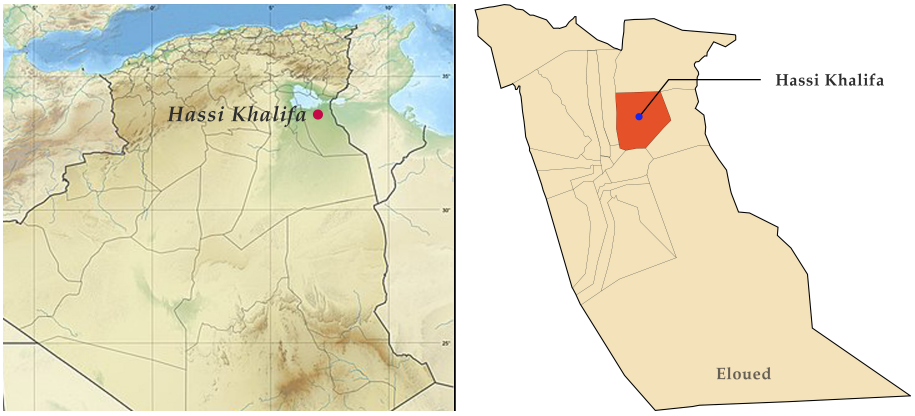

FIGURE 2.2: Hassi Khalifa geographical position in Eloued and Algeria (Source: Wikipedia)

Also, with the use of Google Maps, we got the following satellite pictures illustrated in the figure 2.3 below.

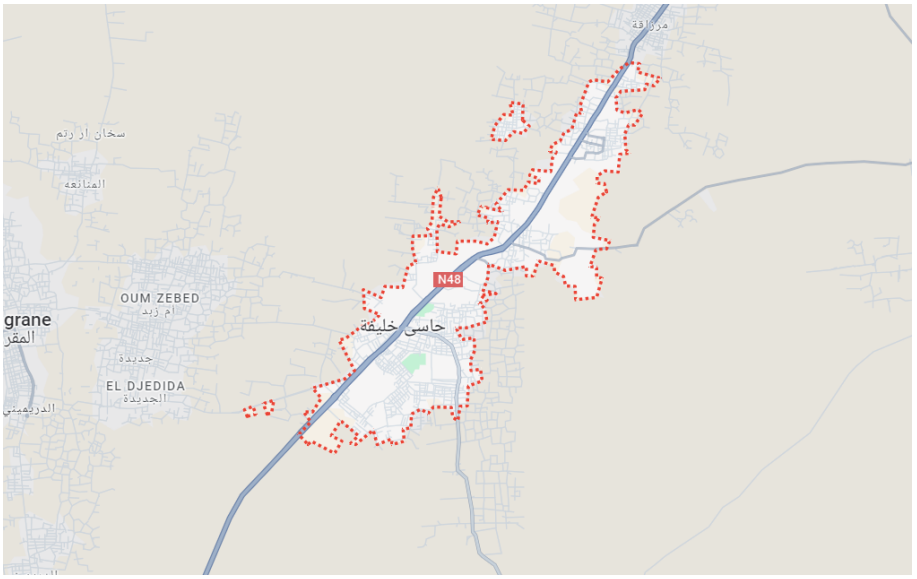

FIGURE 2.3: Hassi Khalifa Geographical Position (Source: Google Maps)

For the metrological conditions available in this region, Pvgis platformer is used to supply the following tables 2.1, 2.2, 2.3 and 2.4 that show the irradiation on the horizontal plane in kWh/m2/mo and the 24-hour average temperature in degrees Celsius.

TABLE 2.1: Monthly solar irradiation estimates for 2019

Mo	Jan	Feb	Mar	Apr	May	Jun	Jul	Aug	Sep	Oct	Nov	Dec	Avg
Irr	110.08	131.83	170.45	214.84	236.92	250.36	252.05	228.67	183.61	151.76	113.54	102.07	178.84

TABLE 2.2: Monthly solar irradiation estimates for 2020

Mo	Jan	Feb	Mar	Apr	May	Jun	Jul	Aug	Sep	Oct	Nov	Dec	Avg
Irr	112.81	138.58	181.91	193.15	231.2	244.21	252.46	230.49	178.5	152.73	116.02	102.45	177.88

TABLE 2.3: Monthly average temperature for 2019

Mo	Jan	Feb	Mar	Apr	May	Jun	Jul	Aug	Sep	Oct	Nov	Dec	Avg
Temp	10.4	11.4	15.6	20.7	24.2	33.0	34.2	33.7	30.3	23.0	14.5	13.3	22.02

TABLE 2.4: Monthly average temperature for 2020

Mo	Jan	Feb	Mar	Apr	May	Jun	Jul	Aug	Sep	Oct	Nov	Dec	Avg
Temp	10.5	14.1	16.7	21.8	27.5	31.4	32.5	33.3	28.2	21.5	16.9	12.2	22.22

As seen from the tables above, The average monthly recorded irradiance for 2019 is about 178.84 Kwh/m2 and 177.88 Kwh/m2 for 2020 with the highest value around July with 252.05Kwh/m2 for 2019 and 252.46 KWH/m2 for 2020. The lowest one was recorded in December at 102.07 KWH/m2, the results are shown in the curve illustrated in figure 2.4 below. For temperature, a peak temperature is recorded in July at 34.2°C for 2019 and 33.3°C for 2020. The lowest temperature was then recorded in January 2020 at 10.5°C, the results are all shown in figure 2.5 below. The data discussed reflects this region's importance in terms of climatic conditions as they make it favorable for generating the maximum power needed for growing crops.

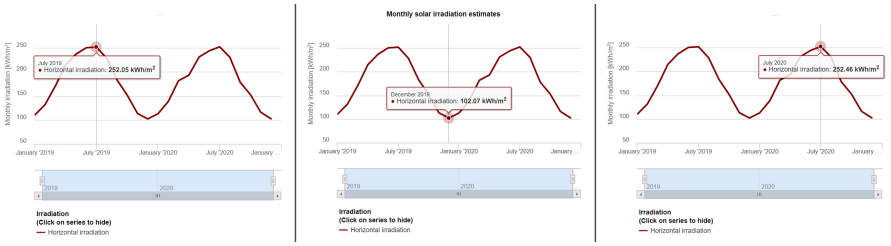

FIGURE 2.4: Monthly solar irradiation between 2019 and 2020 (Source: PVgis)

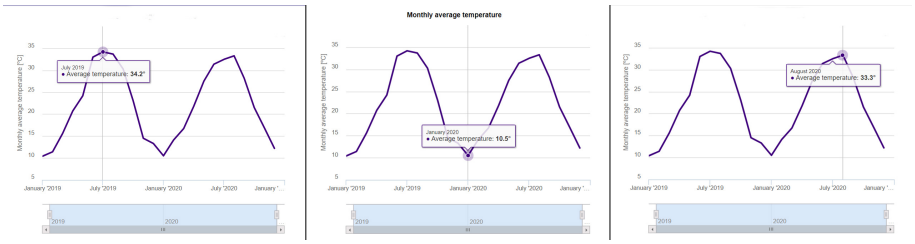

FIGURE 2.5: Monthly solar temperature between 2019 and 2020 (Source: PVgis)

Additionally, another table 2.5 was recorded for Eloued temperature from **?**, the reason is due to the accurate yet detailed data this table supplies compared to the one from Pvgis, which might be super helpful when sizing the motor-pump system.

TABLE 2.5: Min. Temperature °C, Max. Temperature °C and Avg. Temperature °C

Mo	Jan	Feb	Mar	Apr	May	Jun	Jul	Aug	Sep	Oct	Nov	Dec
Avg Temp	10.56	12.78	16.67	21.11	26.11	30.56	33.89	33.33	28.89	23.33	16.11	11.11
Min Temp	5.5	7.2	10.5	15.0	19.4	23.0	26.6	26.6	22.7	17.2	11.1	6.6
Max Temp	16.6	18.8	22.7	27.2	32.2	37.2	40.0	39.4	35.0	28.8	22.2	17.2

Figure 2.6 is also attached to this table for better data understanding.

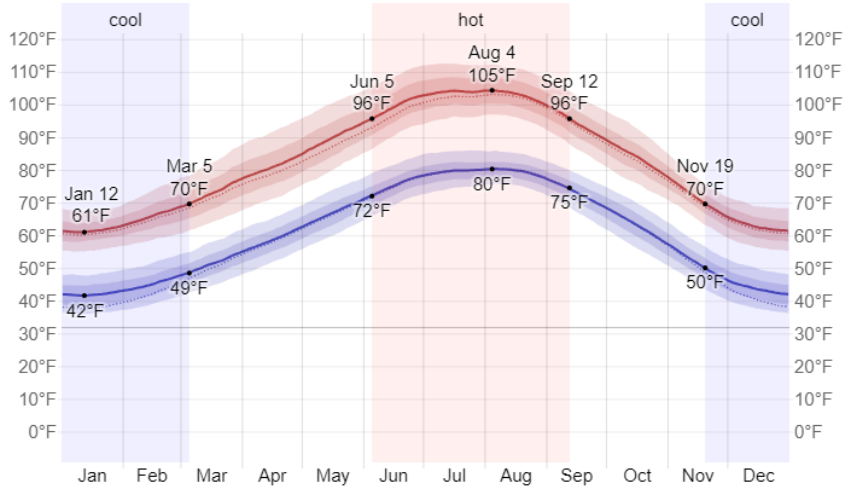

FIGURE 2.6: Average High and Low Temperature in °F for El Oued (Source: Weather Spark)

More data has been recorded from **?** including Rainfall in mm, Humidity in %, wind speed in Km/day, and average Sun hours. The data records are within table 2.6 along with figure 2.7 all shown below.

TABLE 2.6: Recorded data for rainfall, Humidity, wind speed, and average Sun hours

Mo	Jan	Feb	Mar	Apr	May	Jun	Jul	Aug	Sep	Oct	Nov	Dec
Humidity	61.0	47.0	39.0	32.0	28.0	25.0	23.0	26.0	36.0	43.0	53.0	63.0
Wind Speed	320.5	336.0	355.3	386.2	401.6	405.5	374.6	339.8	328.3	305.1	305.1	308.9
Sun Hours	8.8	9.6	10.5	11.5	12.4	12.9	12.7	12.0	11.1	10.1	9.2	8.6
Rain	10.6	5.1	7.6	7.6	2.5	2.5	2.5	2.5	5.1	5.1	7.6	5.1

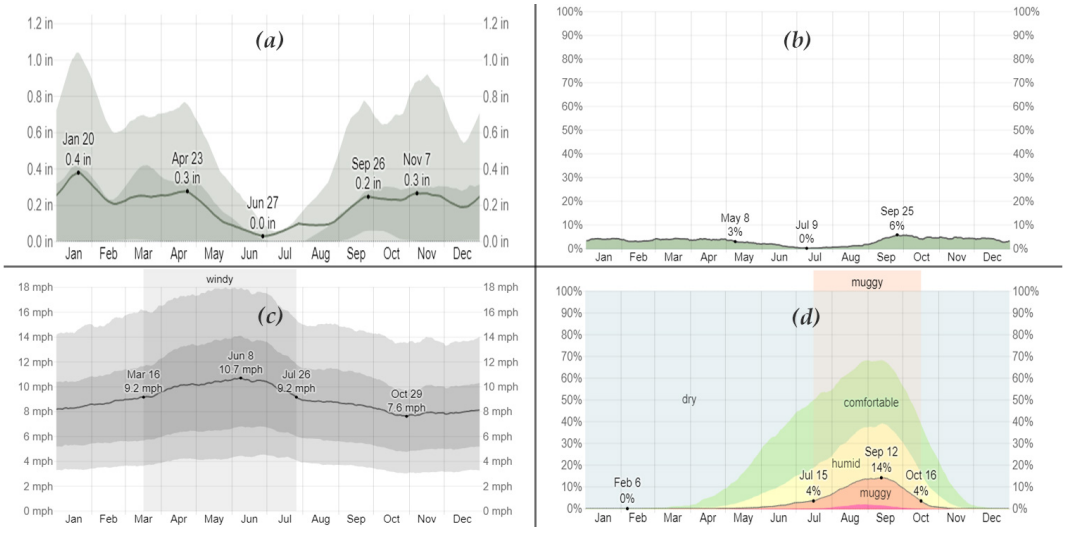

FIGURE 2.7: Climate in Eloued: (a) Average Monthly Rainfall, (b) Daily Chance of Precipitation, (c) Average Wind Speed, and (d) Humidity Comfort Levels (Source: Weather Spark)

In terms of the climatic conditions shown in different tables and figures above, is worth noticeable that the region of Eloued specifically Hassi khalifa is ideal for our SWPS installation, not only because it provides some good amounts of irradiance and sun hours, but also it maximizes the output of our PV array system, which leads to fewer water shortages in irrigation applications. Though as the VIA-MICHELIN platform states, Hassi Khalifa has good connectivity to the grid, this region still experiences electricity interruptions, particularly due to extreme heat events that can stress the electricity distribution network, also the increased demand for cooling during heatwaves strain the grid, leading to power outages **?**, that is why a stand-alone or an off-grid SWPS seem as the best option in this area as it ensures more reliability and cost-effectiveness.

2.2 Motor-Pump System Sizing:

In this chapter section a detailed methodology is presented to achieve an adequate sizing of the stand-alone SWPS utilized in the proposed site discussed in the previous section.

2.2.1 Basic data for pump sizing:

The following data is necessary to size the solar pump and its components, as some of it may have a huge effect on avoiding the system's oversized design which may lead to some water-wasting actions.

2.2.1.1 The flow rate:

The flow rate (Q) is the quantity of water that the pump can deliver during a given interval of time. In pumping, the flow rate is usually given in liters per hour (l/h) or gallons per hour (gph). In solar pumping, the flow rate (or water requirement) is often expressed in cubic meters per day **?**. The literature proposed different ways to find how much flow rate is needed, in **?** the author suggested a simple way to find the daily water consumption for an average farm located in Riyadh, Saudi Arabia, the proposed equation is as follows:

$$\frac{Number\ of\ crops \cdot Consumed\ water\ per\ a\ tree}{Water\ consumption\ percentage\ per\ crop} \tag{2.1}$$

Though equation 2.1 seems to be easy to implement since little data is included in it, it still gives some inaccurate results that may result in the system being oversized. The author in **?** proposed another way for water demand calculations based on the reference evapotranspiration ETo and Crops coefficient kc. The crop coefficient depends on the type and growth stage of the crop. The daily reference evapotranspiration depends on metrological data, it has been estimated using the Penman-Monteith equation **?**:

$$ET_0 = \left(0.408\Delta(R_n - G) + \frac{900}{T+273}u_2(e_s - e_a)\right)\left(\frac{1}{\Delta + \gamma(1 + 0.34u_2)}\right) \tag{2.2}$$

Rn is net radiation at the crop surface (MJ · m2 · day1), G soil heat flux density (MJ · m2 · day1), T mean daily air temperature at 2 m height (°C), u2 wind velocity at 2 m height (ms1), es and ea saturation and actual vapor pressure (kPa), slope of vapor–pressure curve (kPa∘C1), psychrometric constant (kPa∘C1). The crop evapotranspiration ETc is determined using the following formula:

$$ET_c = k_c \cdot ET_o \tag{2.3}$$

This method as shown from equations 2.2 and 2.3 above is a bit complex since it requires more data and computations compared to the previous one, however, the results found here are more accurate, which ensures an adequate system design with less or no oversizing.

Due to the lack of some of the required parameters used in equation 2.2 which are found using some sophisticated apparatus, two software then are used as alternatives which are Cropwat and Climwat. These software are developed by Food and Agriculture Organisation of the United Nations, Cropwat is mainly used as an all-in-one software, and it is based on Climwat, as the latter works as a database generator for a certain selected region, which later could be imported into Cropwat for doing further needed calculations. Cropwat also helps the user manage his crop data throughout the growing process and till the harvest season with curves generating feature, this might be helpful, especially for farmers with no technical background. The following figure 2.8 below shows Cropwat's software interfaces. As seen

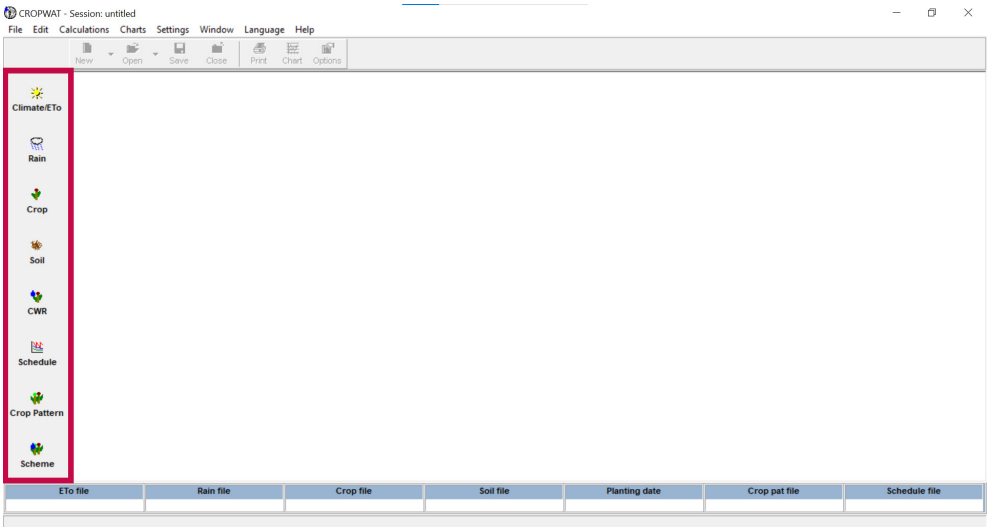

FIGURE 2.8: Cropwat software interface

in figure 2.8 above, the side menu highlighted in red borders shows different options that the Cropwat software does, from supplying climatic data, scheduling the crop growing process and even following the crop pattern. The Climwat software demonstrates how based on a chosen location a database of different crop-related data is generated afterwards which could be inserted later into Cropwat. In our case, Algeria is selected from the country list then by choosing the display all stations within the selected country we get the following window illustrated in figure 2.9 below

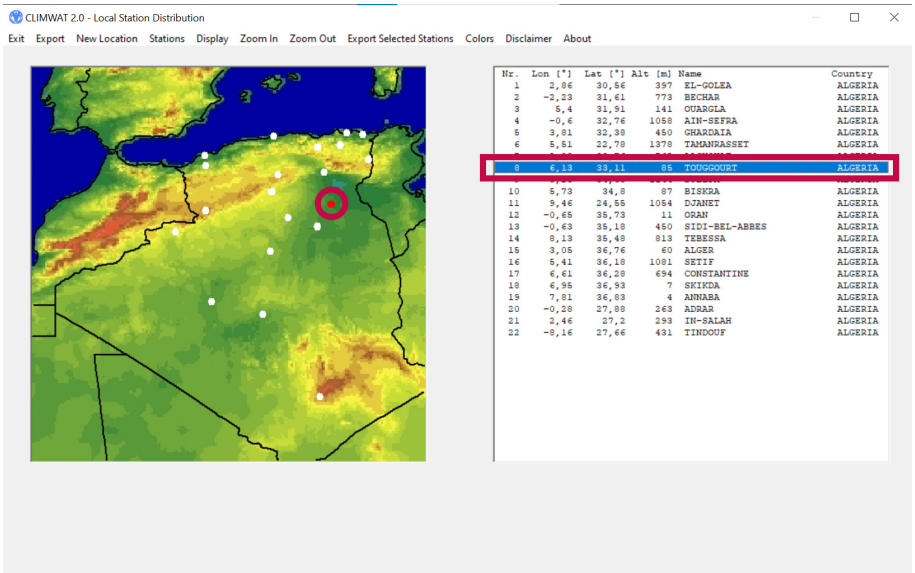

FIGURE 2.9: List of stations within Algeria

From the displayed list of stations, we notice that Eloued region is missing, Touggourt which is situated in ELoued is found instead, hence using the database from Climwat would make it inaccurate that is why data is generated instead from online sources mentioned in Section 1. Moving now to Cropwat software, data will be inserted manually from the tables presented in previous Sections of this Chapter, figure 2.10 then shows a table taken from Cropwat with all the data summarized in it, along with the calculated daily radiation and the reference evapotranspiration ETo inserted in table 2.7

Month	Min Temp	Max Temp	Humidity	Wind	Sun	Rad	ETo
	°C	°C	%	km/day	hours	MJ/m²/day	mm/day
January	5.5	16.6	61	320	8.8	13.4	2.55
February	7.2	18.8	47	336	9.6	16.7	3.78
March	10.5	22.7	39	355	10.5	21.1	5.40
April	15.0	27.2	32	386	11.5	25.3	7.48
May	19.4	32.2	28	401	12.4	28.1	9.46
June	23.0	37.2	25	405	12.9	29.2	11.11
July	26.6	40.0	23	474	12.7	28.6	12.90
August	26.6	39.4	26	340	12.0	26.4	10.48
September	22.7	35.0	36	328	11.1	22.7	8.24
October	17.2	28.8	43	305	10.1	18.2	5.75
November	11.1	22.2	53	305	9.2	14.2	3.70
December	6.6	17.2	63	309	8.6	12.3	2.46
Average	15.9	28.1	40	355	10.8	21.4	6.94

FIGURE 2.10: Different climatic data in the region of Hassi Khalifa, Eloued

TABLE 2.7: Daily radiation and reference evapotranspiration data

Rad ($MJ/m^2/day$)	13.4	16.7	21.1	25.3	28.1	29.2	28.6	26.4	22.7	18.2	14.2	12.3	21.4
ETo (mm/day)	2.55	3.78	5.40	7.48	9.46	11.11	12.90	10.48	8.24	5.75	3.70	6.94	6.94

The figure 2.11 below illustrates the change in daily radiation and reference evapotranspiration expressed in bars curve

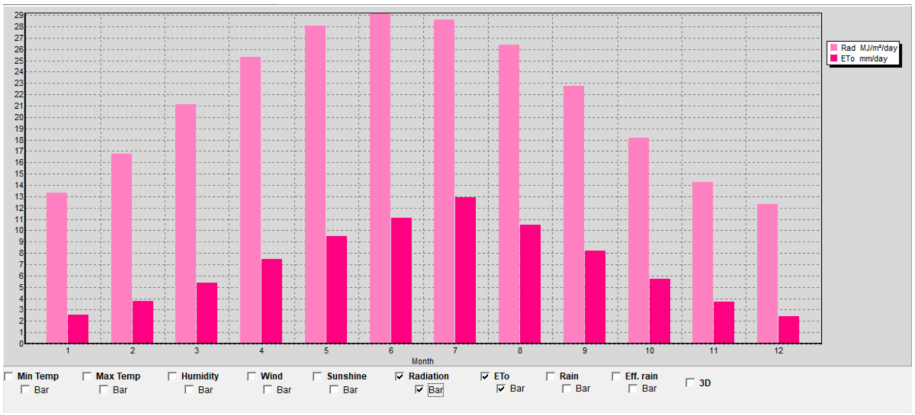

FIGURE 2.11: Daily radiation and reference evapotranspiration changes in the region of Hassi Khalifa, Eloued

It is well noticed from the bar curve above that both the radiation and reference evapotranspiration have peak values in July, with relatively small values for the rest of the months, with an average daily radiation of 21.4 MJ/m^2/day and an average reference evapotranspiration ET0 of 6.94 mm/day. Crop coefficient (Kc) on the other hand, ranges typically from 0.30 to 1.20, depending on the crop type, variety, and developmental stage. These values are essential for calculating the actual crop evapotranspiration ETc. Now, for our selected site in Hassi Khalifa, potatoes are planted as the main crop in a 1-hectare rounded land, with 10cm between each crop, which makes a total of 10,000 potatoes harvested in every 2 main seasons; autumn season (Sep-Dec) and spring season (Feb-May). In our case, the autumn season is selected for potato growing which goes through 4 main stages:

1. Initial Stage: lasts from September to the beginning of October. Few amounts of water are required in this stage since the potato crop is in its first growing state.

2. Developing Stage: lasts from October to the beginning of November. High amounts of water are required in this stage since the potato crop is in its developing state.

3. Mid Stage: lasts from the middle of November to December. water demand starts decreasing as we approach the final stage

4. Late Stage: lasts from December to January. smaller amounts of water are needed here since the potato crop is almost ready to be harvested.

The crop coefficient Kc for potatoes then ranges between 0.5 to 1.15 with some tolerances around the minimum and maximum values as shown in figure 2.12 below taken from Cropwat software

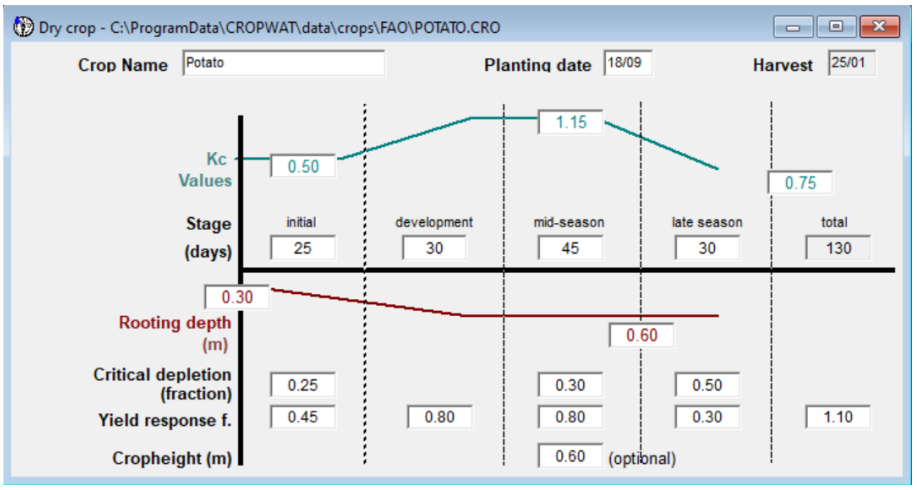

FIGURE 2.12: Crop coefficient curve for potatoes crop

We notice from the curve illustrated above in figure 2.12 that the crop coefficient has the highest value around the mid-season stage where more water is demanded.

After finding both the crop coefficient and the reference evapotranspiration, which through the use of equation 2.3 helps finding the actual evapotranspiration ETc. The figure 2.13 below contains a table with all necessary data generated using Cropwat software, along with a curve illustrated in figure 2.14 which shows the change in required irrigation in mm per decade for the autumn season.

Month	Decade	Stage	Kc	ETc	ETc	Eff rain	Irr. Req.
			coeff	mm/day	mm/dec	mm/dec	mm/dec
Sep	2	Init	0,50	4,12	12,4	0,4	12,4
Sep	3	Init	0,50	3,71	37,1	1,4	35,7
Oct	1	Init	0,50	3,29	32,9	1,3	31,6
Oct	2	Deve	0,58	3,35	33,5	1,3	32,1
Oct	3	Deve	0,82	4,14	45,5	1,5	44,0
Nov	1	Deve	1,05	4,62	46,2	1,9	44,3
Nov	2	Mid	1,18	4,36	43,6	2,2	41,4
Nov	3	Mid	1,18	3,87	38,7	1,9	36,8
Dec	1	Mid	1,18	3,30	33,0	1,4	31,6
Dec	2	Mid	1,18	2,77	27,7	1,1	26,6
Dec	3	Late	1,16	2,81	30,9	1,7	29,2
Jan	1	Late	1,04	2,55	25,5	2,6	22,9
Jan	2	Late	0,91	2,23	22,3	3,2	19,1
Jan	3	Late	0,81	2,35	11,7	1,2	10,4
					441,0	**23,2**	**418,1**

FIGURE 2.13: Seasonal irrigation data for potatoes crop management

As seen from figure 2.14 above, there are different water demand levels throughout the autumn season, with a peak in November at 44.3 mm/dec, based on that and given that the area being irrigated is 1 hectare (which is $10,000$ m^2), the conversion from millimeters per decade to cubic meters per day is calculated as follows:

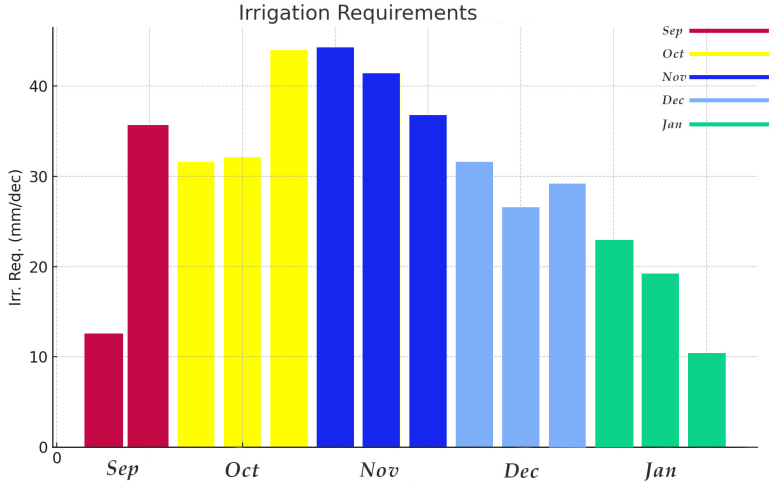

FIGURE 2.14: change in required irrigation in mm per decade for the autumn season

1. Convert millimeters to meters:

$$44.3 \text{ mm} = 0.0443 \text{ m}$$

2. Calculate the total volume of water per decade:

$$\text{Volume per decade} = \text{Area} \times \text{Height}$$

$$\text{Volume per decade} = 10,000 \text{ m}^2 \times 0.0443 \text{ m} = 443 \text{ m}^3$$

3. Convert the volume per decade to volume per day:

$$\text{Volume per day} = \text{Volume per decade}/10$$

$$\text{Volume per day} = 443 \text{ m}^3/10 = 44.3 \text{ m}^3/\text{day}$$

Thus, for an area of 1 hectare, the irrigation requirement of 44.3 mm per decade corresponds to 44.3 cubic meters per day, we take it approximately 44 cubic meters per day. The peak sun hours are illustrated in figure 2.15 below
From the curve above, a PSH (Peak Sun Hour) is defined as 10.8, taking the average of all sun hours during 12 months.

To find the flow rate now, the following equation is used:

$$Q = \frac{Q'}{\text{PSH}}(\text{m}^3/\text{hr}) \tag{2.4}$$

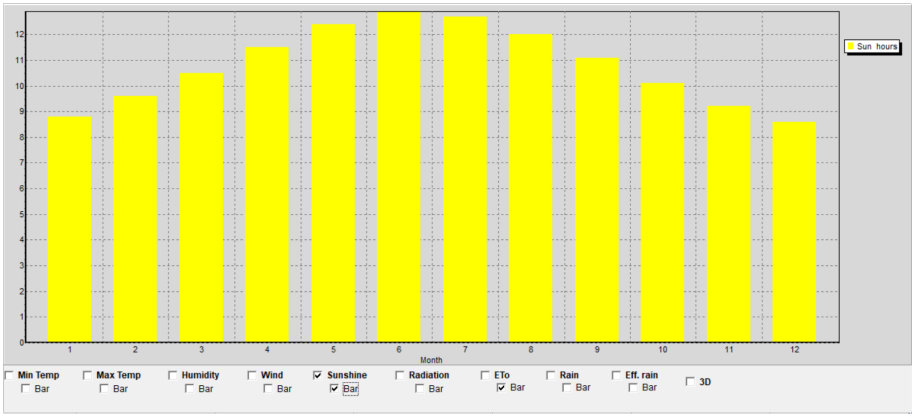

FIGURE 2.15: Peak sun hours bar chart

with Q' equal to the peak required irrigation in m3/day which is 44 is divided on the PSH at 10.8 to convert from cubic meter per day to cubic meter per hour which is the standard unit for the flow rate, results are shown in the equation 2.5 below:

$$Q = \frac{44}{10.8} = 4.08\,\mathrm{m}^3/\mathrm{hr} \approx 4\,\mathrm{m}^3/\mathrm{hr} \tag{2.5}$$

From the results above we see that a 4 m3/hr is a sufficient water volume to meet our site requirements, by producing a good amount of potatoes during the harvesting season, which is the supreme goal of our stand-alone SWPS.

2.2.1.2 Total Dynamic Head (TDH):

The author in **?** defines the total dynamic head (TDH) of a pump as the difference in pressure in meters of water column between the suction and discharge ports. This height can be calculated as shown in equation 2.6:

$$TDH = Hg + Pl \tag{2.6}$$

Where
Hg = is the geometric height between the surface of our submersible pump and the top of our tank (Hd+Ht) as shown in figure 2.16 below

Pl = is the pipe loss caused by the friction of water against the walls of the pipes. These losses depend on the pipes' length, diameter, and the pump's flow rate (Q) and are expressed in meters of water. Generally, these pressure losses correspond to no more than 10% of the total geometric height (Hg).
Now, for the region of El Oued, the depth of underground water resources can vary significantly. In urban areas like El Oued and Kouinine, the depth of shallow aquifers is generally

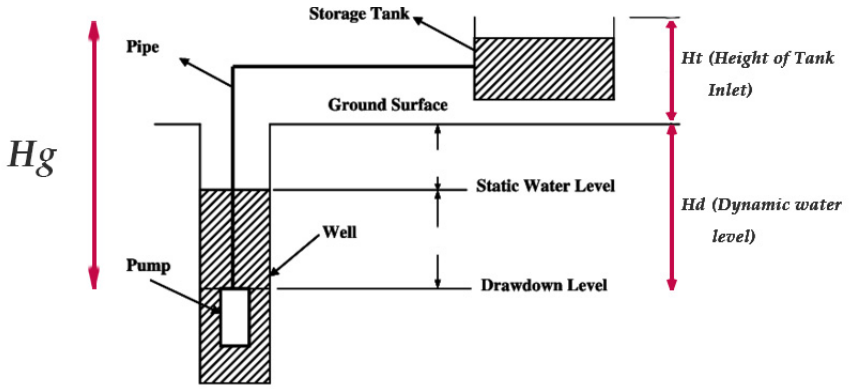

FIGURE 2.16: Static and total dynamic head

between 0.65 and 17.4 meters. However, deeper aquifers in the wider region can be much more substantial. This means groundwater sources can be found at depths exceeding 250 meters below the ground surface, sometimes making it difficult to extract it from such deeper levels **?**. For the site selected in our case, the water is found at depths ranging from 60 up to 80m, we take then 70m as a fixed depth. The tank height is also an important factor to take while calculating for the TDH, as in our case a total of 4m is taken as a tank height divided into 1m for the support and 3m for tank height, figure 2.17 shows a good illustration on the tank's height.

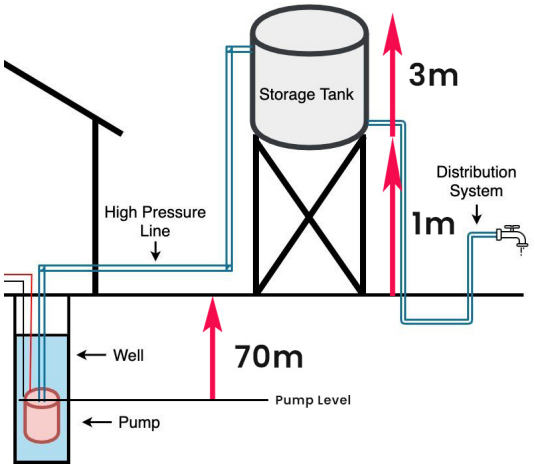

FIGURE 2.17: Water depth and tank height

For the pressure losses it is taken as 10% of the geometric height Hg, now by substituting in equation 2.6 we get the following result for the TDH shown below:

$$\text{TDH} = (70 + 4) \times (1 + 0.10) = 81.4m \tag{2.7}$$

So from equation 2.7 above, we got a TDH of 81.4m, which is needed for our next step; the motor-pump system sizing. For the tank size, the following equation could be used:

$$\text{Tank Size} = \text{Daily Water Needs} \times \text{Number of Backup Days} \tag{2.8}$$

So the daily water need in our case is 44 m3 per day, for the number of backup days, and based on the site selected we take it for 3 days, results are shown below:

$$\text{Tank Size} = 44 \times 3 = 132\text{m}^3 \tag{2.9}$$

Adding a 20% safety margin:

$$\text{Tank Size} = 132 \times 1.2 = 158.4\text{m}^3 \tag{2.10}$$

Hence our tank could save up to 158.4 m^3 of water, which could be used for different purposes; irrigation, domestic, etc.

2.2.2 Motor-pump sizing:

In this section, we focus most on sizing the motor-pump system that would deliver the required amount of water based on the data found in the previous section above. From **?** the author calculated the hydraulic power of the pump using the following equation:

$$P_h = \frac{Q \cdot \rho \cdot g \cdot TDH}{3600 \times 1000} \tag{2.11}$$

Where
P_h is the hydraulic power (Kw).
Q represents the flow rate (m^3/hr).
ρ is the water density (1000 kg/m^3)
g is the acceleration due to gravity (9.81 m/s^2).
TDH is the total dynamic head.
The denominator 3600×1000 converts the units appropriately, typically from cubic meters per second to cubic meters per hour and from watts to kilowatts.

Now, by using the standard values for our flow rate and total dynamic head from Grandfos, we get a 4.32 m^3 and 81.4m standard values for both flow rate and TDH, substituting in equation 2.11, we get the results shown below:

$$P_h = \frac{4.32 \cdot 1000 \cdot 9.8 \cdot 81.4}{3600 \times 1000} = 0.957Kw \tag{2.12}$$

For the motor size, the same author from **?** suggested the equation used below with an assumed motor-pump efficiency equal to 75%:

$$P_m = \frac{P_h}{\eta_{mp}} \tag{2.13}$$

where P_m is the motor power (electric power)
P_h is the hydraulic power
η_{mp} is the motor-pump efficiency

Another author at **?** takes the motor-pump efficiency in a range between 30% to 45% based on the type of pump and motor, which seems more logical compared to an efficiency of 75%, therefore, a standard efficiency of 44.3% is taken -based on the flow rate and TDH- for the motor-pump system used in our case, we get then the following results:

$$P_m = \frac{0.957}{44.3\%} = 2.16\,\text{Kw} \approx 2.2\,\text{Kw} \tag{2.14}$$

We see from equation 2.14 that the required electrical power by the motor is 2.2Kw whereas the hydraulic power found from equation 2.11 is 0.957Kw, this way the motor-pump system is sized to deliver the needed amounts of water, additionally we could use the grandfos catalogue to pick a submersible water pump based on the sized parameters found above.

For the inverter, it is sized based on the motor power, which is found to be 2.2Kw, considering a small margin of about 30% to ensure the inverter's ability to handle the power sparks. The equation below illustrates the inverter sizing:

$$P_{\text{inv}} = P_m \cdot (1 + 30\%) = 2.86\,\text{Kw} \approx 3\,\text{Kw} \tag{2.15}$$

Now, for the Pv array, we do the same thing, only this time it would be sized based on the inverter power instead of the motor power. From equation 2.15 the inverter power calculated is 3Kw, adding a margin of 5% in this case, we get:

$$P_{\text{pv}} = P_{\text{inv}} \cdot (1 + 5\%) = 3.15\,\text{Kw} \tag{2.16}$$

So, by choosing a PV module of 320W, the following number of modules is found:

$$\text{Number of PV modules} = \frac{3.15}{0.319} = 9.9 \approx 10\,\text{module} \tag{2.17}$$

In our case, we take 10 modules for our PV array, they are all installed in series to meet the voltage and current requirements. for the DC bus voltage we take it as 680 v to meet the input voltage for our inverter.

2.3 Conclusion

In this chapter we have discussed the SWPS sizing, starting by identifying the fundamental data needed for defining the motor-pump system, afterward, an inverter, PV array, and DC bus voltage were selected based on the motor selected.

Chapter 3

Modeling and Design of the system

Introduction

In this chapter, a complete modeling of the stand-alone solar water pumping system will be realized, including all the components necessary for the system's performance under different conditions. Starting with the PV array, which is considered as a main source of energy in stand-alone systems, followed by a DC to DC boost converter used for stepping up the voltage, incorporated with an Mppt controller for maximum power point tracking (MPPT) of the PV. The DC-DC converter is connected to a three-phase inverter controlled by DTC algorithm to drive the IM motor which in return is coupled with a centrifugal pump that converts the mechanical energy to hydraulic energy.

3.1 Photovoltaic panel modeling:

3.1.1 The working principle of PV cells:

Since Solar energy is the most affordable and abundant of all long-term natural resources to date **?**, the use of Solar PV technology has become then one of the optimum ways to utilize solar power in generating electricity for different applications. A PV cell is the essential unit of a solar energy generation system where the sunlight photons falling on its surface are directly converted to electrical energy or more specifically to direct current which is used afterward to supply AC or DC loads. The solar cell is a p-n junction device based on electronic semiconductors, particularly crystalline silicon (c-Si) or thin-film semiconductor materials **??**. The n-type refers to the negatively charged electrons donated by donor impurity atoms and the p-type refers to the positively charged holes created by acceptor impurity atoms **???**.

The electricity generation starts When light photons hit a cluster of solar cells, as a result, they excite electrons into a higher energy state, making them act as charge carriers in an electrical current. In other words, solar energy impacts the cells, causing their atoms to absorb photons from sunlight, which then excite and release electrons, that in return create electron-hole pairs. These electrons travel through a conductor, creating an electrical current that directly corresponds to the intensity of sunlight received by the collector **?**. Figure 3.1 shows a p-n junction of PV cell

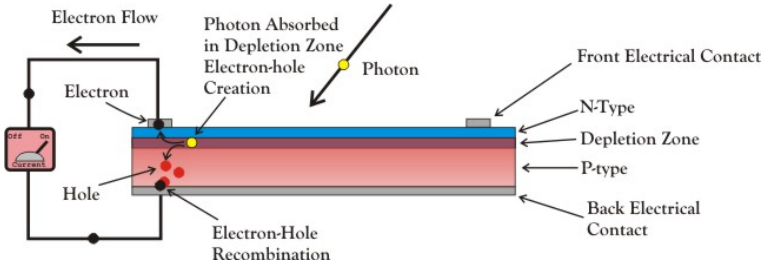

FIGURE 3.1: p-n junction of PV cell

So, as seen from figure 3.1 above, the photon's absorption in the depletion region will lead to the creation of electron-hole pairs, which results in direct current flowing in the conductor.

Usually PV cells are constructed from two essential types of crystalline materials, monocrystalline and multi-crystalline solar modules. Single-crystal semiconductors have superior electrical characteristics (20% efficiency) comparable to polycrystalline materials. Nevertheless, monocrystalline PV modules are non-economical as crystalline wafer-based technology is too expensive **??**. There exist also PV cells constructed from thin-film semiconductor materials. All the types are shown in figure 3.2 below.

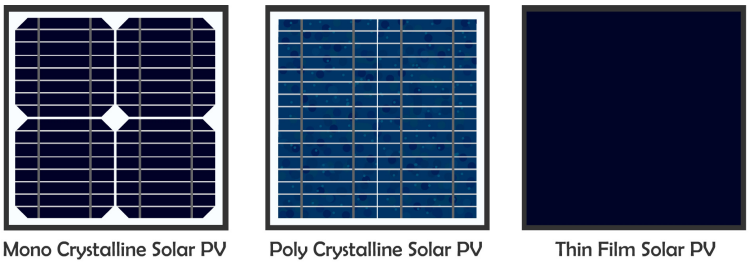

FIGURE 3.2: PV cells different construction types

A typical photovoltaic (PV) cell produces a voltage of approximately 0.5 to 0.6 volts under open-circuit conditions. This voltage range is a standard feature of most silicon-based solar cells today. Now to achieve useful voltages and currents suitable for real-world applications, multiple PV cells are connected whether in series or parallel to form a PV module, which when connected in series produces a string that has a stable current but a higher voltage.

Multiple strings can be connected afterward in parallel to increase the current capacity of the installation without increasing the voltage beyond the desired level, this gives a PV array, which refers to the complete set of panels (both series and parallel connections) installed to meet the energy requirements of a particular application. Figure 3.3 below shows the different PV configurations, starting from a basic cell and going up to more complex installations; PV array.

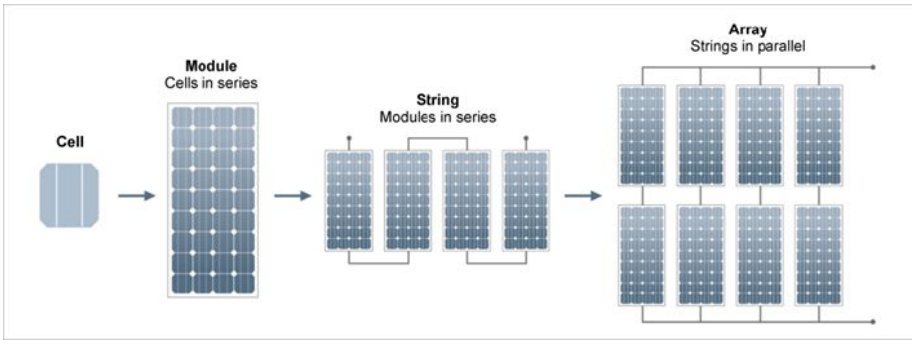

FIGURE 3.3: Different PV configurations

3.1.2 Mathematical equivalent circuit for photovoltaic cell:

A PV cell is the basic component of a PV generator, and it can be modeled using various approaches based on how accurately it matches a real-world PV cell. There exist different equivalent circuits, all used for modeling the output characteristic of a PV cell, in our case, a single diode model is used since is the simplest one, and it has a good output efficiency too. Additionally, the literature has mentioned other types of equivalent circuits for instance the double-diode PV cell model which in **?** seems to have better output efficiency compared to a single-diode model, but still, the latter is much better due to its simplicity. figure 3.4 illustrates the equivalent circuits for both single and double-diode models.

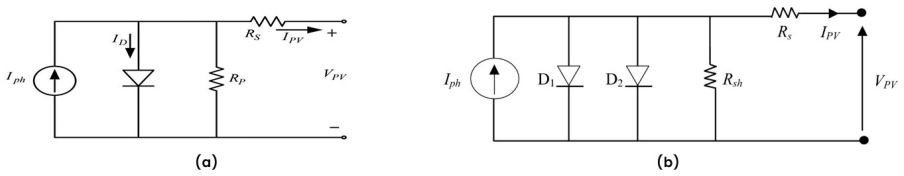

FIGURE 3.4: PV cell equivalent circuit: (a) single-diode model (b) double-diode model

Now, focusing on the single-diode equivalent circuit of the PV cell shown above, one could notice that it contains a current source labeled as I_{ph} which is the cell photocurrent in parallel with a diode, these two represent an ideal PV cell model. For a practical PV cell model, two resistances are added; R_{sh} and R_s which are the intrinsic shunt and series resistances of the cell, respectively **?**. Usually, the value of Rsh is very large and that of Rs is very small, hence they may be neglected to simplify the analysis **?**. Figure 3.5 below shows the ideal and practical PV cell equivalent circuit.

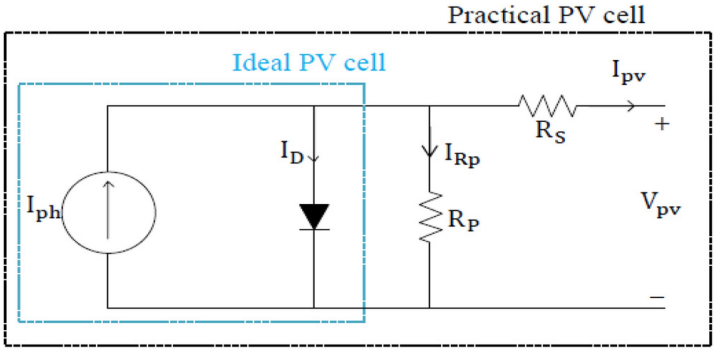

FIGURE 3.5: Ideal and practical PV cell equivalent circuit

The development of this model is based on the equations in **?** from 3.1 to 3.6 shown below, extracted from the single-diode equivalent circuit shown above using some basic electrical rules, taking into account the effects of solar irradiation and temperature changes.
Module photo-current I_{ph}:

$$I_{ph} = (I_{sc} + K_i(T - 298)) \times \frac{I_r}{1000} \tag{3.1}$$

Here,
I_{ph}: photo-current (A),
I_{sc}: short circuit current (A),
K_i: short-circuit current of the cell at 25 °C and 1000 W/m2,
T: operating temperature (K),
I_r: solar irradiation (W/m2).

Module reverse saturation current I_{rs}:

$$I_{rs} = \frac{I_{sc}}{\exp\left(\frac{qV_{OC}}{N_S kT}\right) - 1} \tag{3.2}$$

Here:
q, the electron charge, equals 1.6×10^{-19} C,

V_{OC}: open-circuit voltage (V),
N_s: number of cells connected in series,
n: the ideality factor of the diode,
k: Boltzmann's constant, equals 1.3805×10^{-23} J/K.

The module saturation current I_0 varies with the cell temperature, which is given by:

$$I_0 = I_{rs} \left[\left(\frac{T}{T_r} \right)^3 \exp \left(\frac{q \times E_{g0} \left(1 - \frac{1}{T_r/T} \right)}{nk} \right) \right] \tag{3.3}$$

Here:
T_r: nominal temperature = 298.15 K,
E_{g0}: band gap energy of the semiconductor, equals 1.1 eV,

The current output of the PV module is:

$$I = N_p \times I_{ph} - N_p \times I_0 \times \left[\exp \left(\frac{V/N_s + I \times R_s/N_p}{n \times V_t} \right) - 1 \right] - I_{sh} \tag{3.4}$$

with

$$V_t = \frac{k \times T}{q} \tag{3.5}$$

and

$$I_{sh} = \frac{V \times \frac{N_p}{N_s} + I \times R_s}{R_{sh}} \tag{3.6}$$

Here:
N_p: number of PV modules connected in parallel,
R_s: series resistance (Ω),
R_{sh}: shunt resistance (Ω),
V_t: diode thermal voltage (V).

In order to make sure that the photovoltaic system meets the voltage and current requirements, a sufficient number of PV cells is connected in series or in parallel to form a PV module. Figure 3.6 from **?** presents the equivalent circuit model of a PV module, along with some necessary changes in the PV cell equivalent circuit equations shown above.

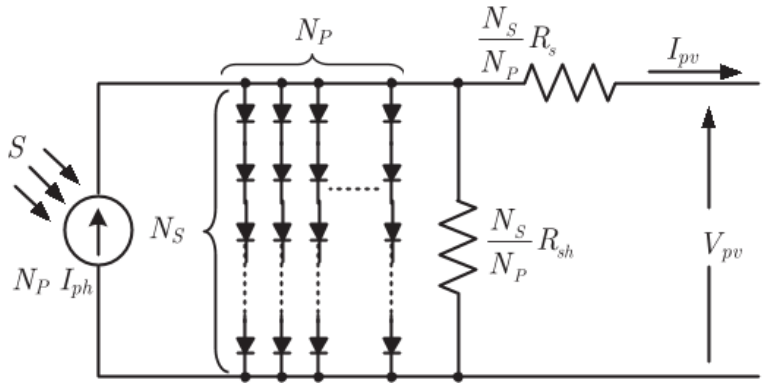

FIGURE 3.6: equivalent circuit model of a PV module

It is seen from the figure above that for N_p cell in parallel and N_s cell in series, we get a total shunt resistance $R_{sh,module}$ and a total series resistance $R_{s,module}$ as shown below:

$$R_{sh,\text{module}} = \left(\frac{N_p}{N_s}\right) \times R_{sh,\text{cell}} \tag{3.7}$$

$$R_{s,\text{module}} = \left(\frac{N_s}{N_p}\right) \times R_{s,\text{cell}} \tag{3.8}$$

Where:

$R_{sh,\text{module}}$: Total shunt resistance (Ω),

$R_{s,\text{module}}$: Total series resistance (Ω),

$R_{sh,\text{cell}}$: Shunt resistance (Ω),

$R_{s,\text{cell}}$: Series resistance (Ω),

N_s: Number of cells in series,

N_p: Number of cells in parallel,

Hence equation 3.4 becomes [cite]:

$$I = I_{ph}N_p - I_0 N_p \left[\exp\left(\frac{V + IR_s\left(\frac{N_s}{N_p}\right)}{aV_T N_s}\right) - 1\right] - \frac{V + IR_s\left(\frac{N_s}{N_p}\right)}{R_p\left(\frac{N_s}{N_p}\right)} \tag{3.9}$$

3.1.3 Temperature and irradiance effects:

In a direct current (DC) electrical circuit, the power is determined by multiplying voltage and current. This relationship is shown in the following mathematical formula:

$$P = V \times I \tag{3.10}$$

Where, P: Power (Watt), V: Voltage (Volt), I: Current (Ampere)

In the case of a PV cell, current and power vary to different values of voltage, giving what is known as the PV cell electrical characteristics which are shown in figure 3.7 below:

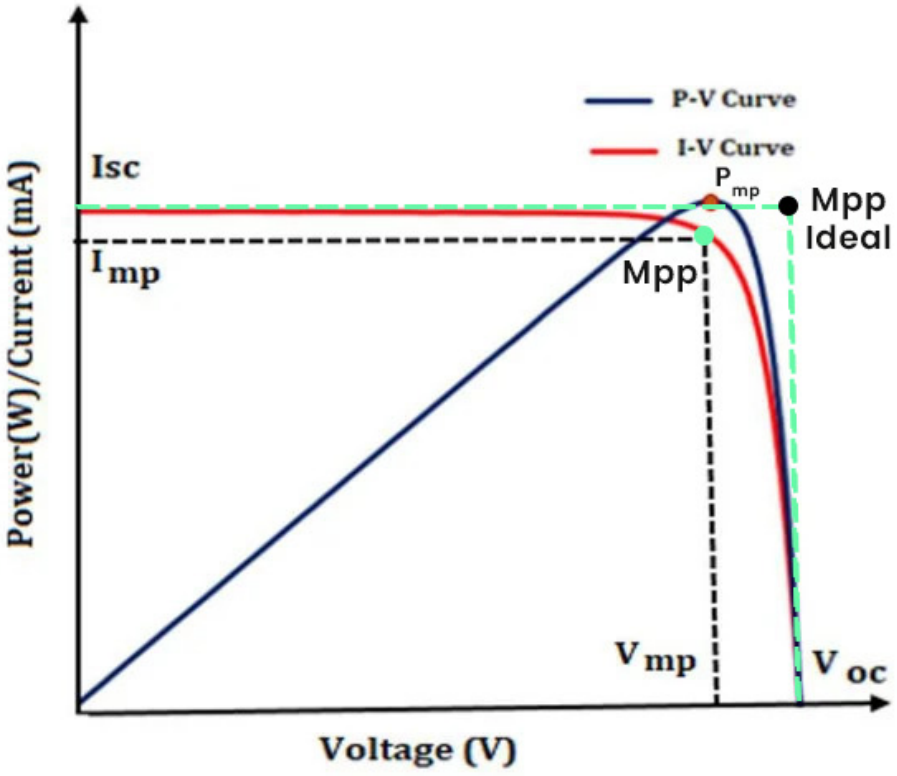

FIGURE 3.7: Photovoltaic electrical characteristics

So, as seen from the figure above, we have two Mpp, an ideal one which appears to be the multiplication of the short circuit current I_{sh} and the open circuit voltage V_{oc}, and another one which is the result of multiplying the maximum point current I_{mp} and the maximum point voltage V_{mp}, hence the ideal Mpp is to be avoided, since in such conditions no current flows in the circuit because it is open. To measure now the PV efficiency which is calculated as the ratio between the power in Mpp (for a specific temperature) and the input power as equation 3.11 shows below [**?**:

$$\eta = \frac{P_{mpp}}{P_{in}} \tag{3.11}$$

Knowing that,

$$P_{in} = A_{\text{cell}} G \tag{3.12}$$

Where,

η: Efficiency

P_{mpp}: Power in Mpp (Watt)

P_{in}: Input power (Watt)

A_{cell}: Cell Area (m^2)
G: Irradiance (W/m^2)

Another important factor is the fill factor of a module, which is a crucial metric that significantly influences its performance comparison among different photovoltaic modules. A module with a high fill factor indicates superior quality, characterized by minimal internal losses. fill factor can be calculated from equation 3.13 below:

$$FF = \frac{P_{\max}}{I_{sc}V_{oc}} = \frac{I_{mpp}V_{mpp}}{I_{sc}V_{oc}} \tag{3.13}$$

Where,
FF: Fill Factor,
P_{max}: Maximum power at Mpp (Watt),
I_{sh}: Short circuit current (Ampere),
V_{oc}: Open circuit voltage (Volt),
I_{mpp}: Current at maximum power point (Ampere),
V_{mpp}: Voltage at maximum power point (Volt).

The performance of photovoltaic (PV) panels is significantly influenced by temperature and irradiance. An increase in cell temperature typically reduces panel efficiency, primarily due to a decrease in the semiconductor's bandgap, which lowers the open-circuit voltage (Voc) and, subsequently, the power output. Conversely, higher irradiance boosts the power output by increasing the generated current, as more photon energy is converted into electrical energy. However, the attendant rise in panel temperature might offset some gains in output due to higher irradiance. Optimizing panel orientation and tilt is essential to maximize energy production, taking into account local sunlight and temperature conditions **?**. Figures 3.8 and 3.9 below show the effect of varying temperature and irradiance on the PV module.

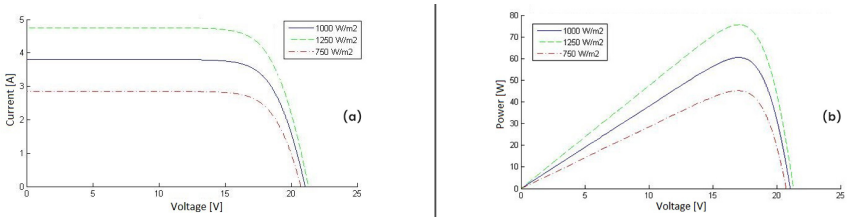

FIGURE 3.8: The effect of irradiance on (a) I-V curve of PV module, (b) P-V curve of PV module

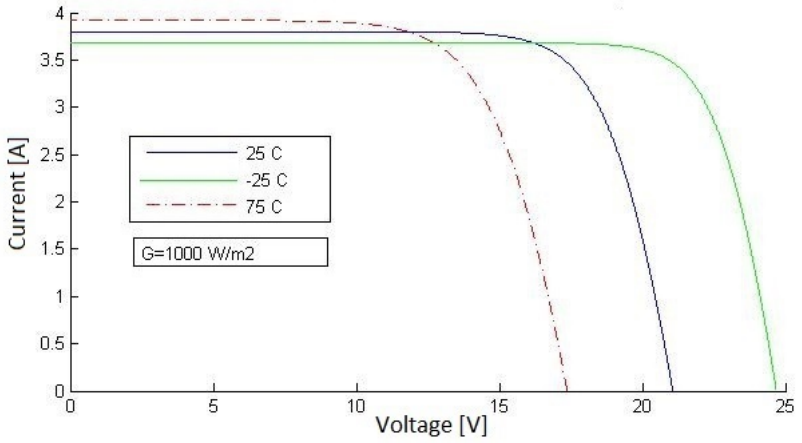

FIGURE 3.9: The effect of temperature on I-V curve of PV module

3.2 Power converters:

Power converters are devices that manage and adjust electrical energy flow by altering current and voltage characteristics to better suit specific applications. They can transform power from AC to DC, DC to AC, DC to DC, and AC to AC. The primary function of power converters is to make the electrical energy output compatible with the power requirements of various loads **?**. For our system, two types of power converters are used; the DC-DC boost converter which is the primary purpose of extracting the Mpp through the use of an MPPT controller, and a voltage source inverter (VSI) to control the operation of the IM.

3.2.1 DC-DC boost converter:

DC-DC power converters are widely used in PV systems as an intermediary between the PV and the load to track the maximum power point (MPP). Different topologies and design approaches could be used for the DC-DC converters. In this part, the DC-DC boost converter is introduced since it is incorporated within our system **?**.

The boost converter, also known as the step-up converter, and as its name implies, this device converts a low unregulated DC voltage which is obtained by the PV array and therefore it will fluctuate due to changes in radiation and temperature, to a highly regulated output voltage, essentially functioning like a reversed buck converter **?**. A graphical model of the boost converter is shown in figure 3.10 below.
As seen from the figure above, the boost converter consists mainly of four components: an Inductor, an Electronic switch, a Diode, and an output capacitor. The converter then can operate in two different modes based on the capacity of the energy-storing device and how

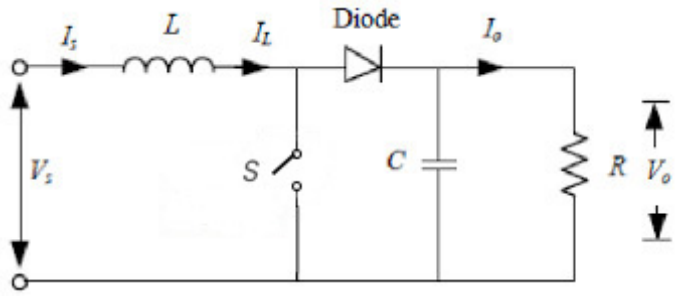

FIGURE 3.10: Circuit Schematic of Step-up DC/DC Converter

long the switching period takes. These two operating modes are known as the continuous conduction mode (CCM), and discontinuous conduction mode (DCM).

3.2.1.1 continuous conduction mode:

Continuous Conduction Mode (CCM) is used for efficient power conversion, and it divides in return to two modes:

- Mode 1: $(0 < t \leq t_{\text{on}})$

In this mode, the switch is turned on at t=0 and terminates at t=t_{on}. Figure 3.11a shows the equivalent circuit for this mode

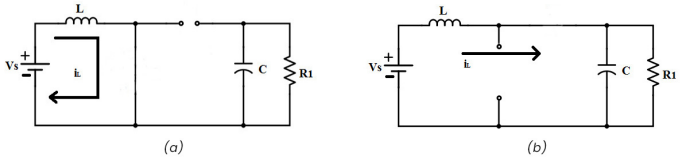

FIGURE 3.11: Equivalent Circuit for boost Converter in CCM

The inductor stores current $i_L(t)$ greater than zero, and ramp up linearly. The inductor takes the same voltage as the source Vi.

- Mode 2: $(t_{\text{on}} < t \leq T_s)$

This mode begins when the switch is turned off at t=ton and terminates at t=Ts. the equivalent circuit for this mode is shown in figure 3.11b above. The inductor current starts decreasing till it reaches zero at t=Ts, then, it starts increasing once again after the switch is turned on during the next cycle. The voltage across the inductor in this mode becomes Vi-Vo. Figure 3.12 below illustrates the inductor current changes during one period cycle.

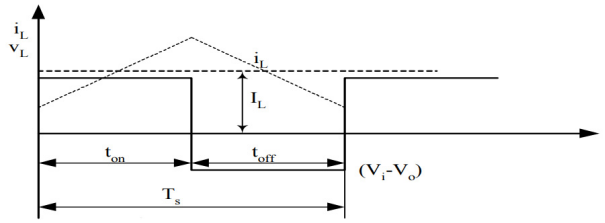

FIGURE 3.12: changes in inductor current through one cycle period for CCM

Now, the time integral of the inductor voltage in steady state over one cycle must equal zero, based on that, equation 3.14 is developed:

$$V_i t_{\text{on}} + (V_i - V_o) t_{\text{off}} = 0 \tag{3.14}$$

Where:

V_i The input voltage, (V).

V_o The average output voltage, (V).

$t_{\textbf{on}}$ The switching on time, (s).

$t_{\textbf{off}}$ The switching off time, (s).

Dividing both sides by T_s and rearranging items yield:

$$\frac{V_o}{V_i} = \frac{T_s}{t_{\text{off}}} = \frac{1}{1 - D} \tag{3.15}$$

Where:

T_s The switching period, (s).

D The duty cycle.

From equation 3.15, we get the following relation from which it is seen that as the duty cycle varies from 0 to 1 our input voltage value is increased to reach a certain output voltage based on the load requirements:

$$V_{\text{out}} = \frac{1}{1 - D} V_{\text{in}} \tag{3.16}$$

Assuming a lossless circuit where P_i=P_o, then

$$I_i V_i = I_o V_o \tag{3.17}$$

We get:

$$\frac{I_o}{I_i} = 1 - D \tag{3.18}$$

Where:

I_o : The average output current, Amp.

I_i : The average input current, Amp.

3.2.1.2 Discontinuons conduction mode:

If the current flowing through the inductor falls to zero before reaching T_s, then the boost converter is said to be operating in the discontinuous conduction mode which is mainly used for low power or stand-by operation, the equivalent circuit for this mode along with the change in inductor current through one period cycle is shown in figure 3.13 below.

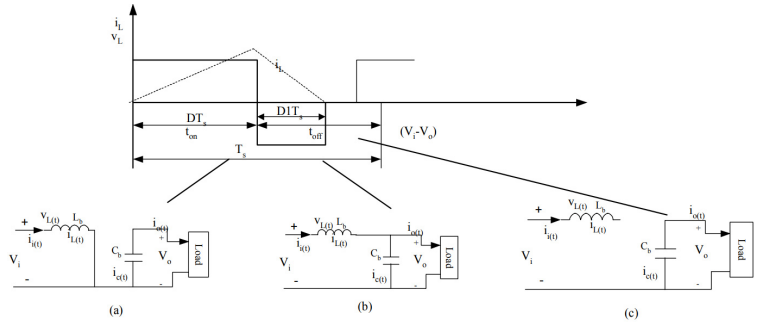

FIGURE 3.13: Equivalent Circuit for boost Converter in DCM: (a) Mode 1, (b) Mode 2, and (c) Mode 3 [Cite paper]

If we equate the integral of the inductor voltage over one time period to zero, we get:

$$V_i DT_s + (V_i - V_o) DT_1 s = 0 \tag{3.19}$$

Then,

$$V_o = \frac{D_1 + D}{V_i D_1} \tag{3.20}$$

$$\frac{I_o}{I_i} = \frac{D_1}{D_1 + D} \quad (\text{since } P_i = P_o) \tag{3.21}$$

3.2.2 Voltage source inverter (VSI):

Inverters in general convert The DC input to an AC output suitable for different load applications. They are classified mainly into two types; voltage source inverters (VSIs) and current source inverters (CSIs)**?**. The main difference lies in the output impedance characteristics. In a voltage source inverter, the output impedance is low, while in a current source inverter, the output impedance is high.

A voltage source inverter is an electronic device that converts a DC (direct current) input voltage into a variable AC (alternating current) output voltage. A VSI is commonly used in various applications, such as adjustable speed drives for electric motors, renewable energy systems (such as solar and wind power), and uninterruptible power supplies (UPS), additionally, it is used for medium to high power applications in contrary to single phase VSI which could be used only in low power applications. Figure 3.14 below demonstrates the electrical circuit of a typical three-phase voltage source inverter

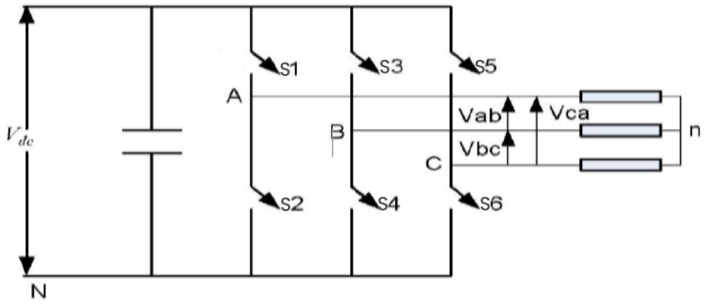

FIGURE 3.14: Power circuit of a three-phase VSI

As seen from the figure above, the VSI has six switches (S1, S2, S3, S4, S5, and S6) which typically are power semiconductor devices (such as MOSFETs or IGBTs). Every two switches in one leg can not be turned ON simultaneously, as this might lead to a short circuit. Hence, the nature of every two switches in the same leg is complementary as equation 3.22 demonstrates:

$$\begin{cases} S_{11} + S_{12} = 1 \\ S_{21} + S_{22} = 1 \\ S_{31} + S_{32} = 1 \end{cases} \tag{3.22}$$

This VSI has eight valid switch states, which are shown in Table 3.1, of these eight states two of them (states 1 and 8) produce zero AC line voltages. The remaining states (states 2 to 7) make a non-zero AC output voltage. The inverter moves from one state to another to generate a given voltage waveform. Thus the resulting AC output line voltages consist of discrete values of V_{dc}, 0, and $-V_{dc}$. The process of choosing specific states to create the

desired waveform involves a modulation technique that ensures only valid states are utilized **?**.

TABLE 3.1: The switching states in a three-phase inverter.

State	S_{11}	S_{12}	S_{31}	V_{ab}	V_{bc}	V_{ca}
1	0	0	0	0	0	0
2	0	0	1	0	$-V_{dc}$	V_{dc}
3	0	1	0	$-V_{dc}$	V_{dc}	0
4	0	1	1	$-V_{dc}$	0	V_{dc}
5	1	0	0	V_{dc}	0	$-V_{dc}$
6	1	0	1	V_{dc}	$-V_{dc}$	0
7	1	1	0	0	V_{dc}	$-V_{dc}$
8	1	1	1	0	0	0

Thus, the line-to-line voltages depend on the switching signals, and the input DC bus voltage are found as shown in equation 3.23 below:

$$\begin{cases} V_{sab} = V_{DC}(S_{11} - S_{21}) \\ V_{sbc} = V_{DC}(S_{21} - S_{31}) \\ V_{sca} = V_{DC}(S_{31} - S_{11}) \end{cases} \tag{3.23}$$

knowing that the stator voltage ensures the following equation

$$V_{sa} + V_{sb} + V_{sc} = 0 \tag{3.24}$$

Hence, we get the following matrix:

$$\begin{bmatrix} V_{sa} \\ V_{sb} \\ V_{sc} \end{bmatrix} = \frac{V_{DC}}{3} \begin{bmatrix} 2 & -1 & -1 \\ -1 & 2 & -1 \\ -1 & -1 & 2 \end{bmatrix} \begin{bmatrix} S_{11} \\ S_{21} \\ S_{31} \end{bmatrix} \tag{3.25}$$

3.3 Induction motor Model:

3.3.0.1 Design and operation of Induction Motor:

The induction motor (IM) is an alternating current machine that is extensively utilized in different industrial applications due to its low cost, high torque density, simple construction, less maintenance, and robustness **?**. Induction motors are of two types; Squirrel Cage which uses a simple rotor structure resembling a squirrel cage, and Wound Rotor (or Slip Ring), which has a rotor with windings that are connected through slip rings to external resistances for starting and control purposes. Moreover, Induction motors e have the armature winding

on the stator, and the field winding on the rotor as Figure 3.15 shows below.

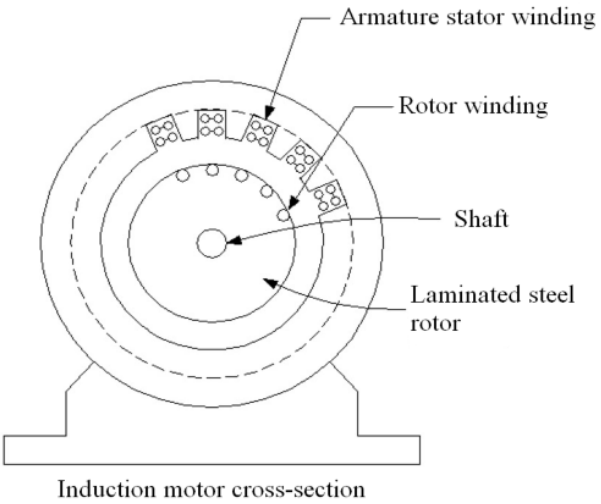

FIGURE 3.15: Induction motor cross section

When a three-phase voltage is applied to the stator winding terminals which might be connected in star or delta, as a result, three-phase balanced currents flow in the armature windings and consequently a rotating magnetic motive force (MMF) field is yielded. This field created in the stator winding rotates at synchronous speed (N_s) in revolution per minute (RPM) such that:

$$N_s = \frac{120f}{P} \tag{3.26}$$

where,

f : Supply frequency and

P : Number of poles.

Based on faraday's law, the rotating stator magnetic field induces voltages in the rotor windings causing balanced currents to flow in the short-circuited rotor. As a result, a rotor MMF is formed, where it rotates with a speed N_r. An electromagnetic torque (Te) is produced due to the interaction between the stator and rotor rotating magnetic fields. The difference of speed between N_r and N_s creates what is called the slip (s) which is defined as:

$$s = \frac{\omega_s - \omega_r}{\omega_s} \tag{3.27}$$

where

ω_s : Synchronous speed in radians per second,

ω_r : Rotor shaft speed in radians per second.

At zero rotor speed (relaxed condition), a unity slip is produced. At synchronous rotor speed, a nil slip is obtained and hence no torque is produced. The motoring operation of IM is typically in the region of $0 < s < 1$ **?**. A typical torque-speed characteristic of an induction motor is shown in Figure 3.16 below.

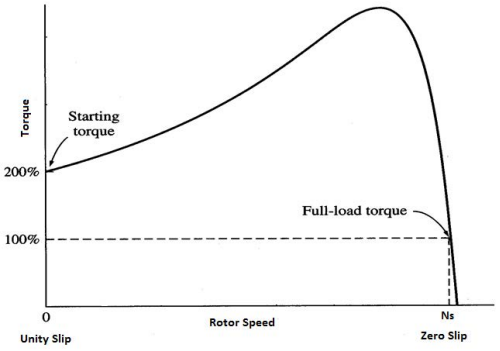

FIGURE 3.16: Typical torque-speed characteristic of IM

3.3.0.2 Mathematical model of Induction Motor:

The winding of the three stator phases and the three rotor phases in space for a symmetrical induction machine can be represented as shown in Figure 3.17. The windings of the stator are identical, sinusoidal distributed, and displaced 120° apart. Similarly, the rotor windings are three identical sinusoidal distributed winding displaced 120° apart. The rotor phases are short-circuited on themselves. There is an electrical angle between the axis of the stator phase (a) and the rotor phase (a).
The following assumptions should be valid to design the mathematical model for IM [cite paper].

1. The stator and rotor windings are represented by stator and rotor resistances (R_s, R_r) respectively.
2. The flux in the stator and rotor are represented by stator and rotor inductances (L_s, L_r) respectively.
3. The interaction between stator and rotor fluxes is represented by mutual inductance (L_m).
4. The air gap between the stator and rotor is uniformly distributed and hence stator and rotor windings are in sinusoidal distribution.

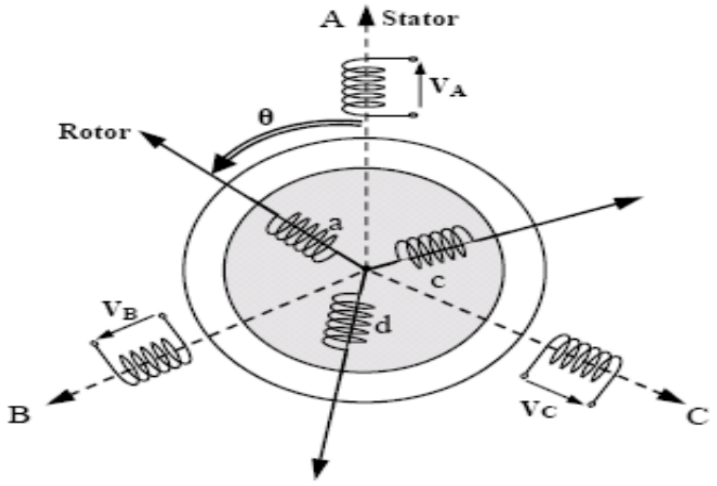

FIGURE 3.17: Representation of stator and rotor windings for an induction motor

5. The motor is running at steady state constant speed. (i.e., $\frac{d\omega_r}{dt} = 0$).

6. The motor is initially relaxed.

3.3.0.3 Electrical equations:

Based on Kirchoff's voltage law, we get the following voltage equations for both stator and rotor windings:

$$v = Ri + \frac{d\Phi}{dt} \tag{3.28}$$

we get then the voltage equation for stator windings as follows:

$$\begin{bmatrix} V_{sa} \\ V_{sb} \\ V_{sc} \end{bmatrix} = \begin{bmatrix} R_s & 0 & 0 \\ 0 & R_s & 0 \\ 0 & 0 & R_s \end{bmatrix} \begin{bmatrix} I_{sa} \\ I_{sb} \\ I_{sc} \end{bmatrix} + \frac{d}{dt} \begin{bmatrix} \Phi_{sa} \\ \Phi_{sb} \\ \Phi_{sc} \end{bmatrix} \tag{3.29}$$

And since resistance R_s is the same for all phases, hence we could write the matrix form shown above in this format:

$$[V_s] = [R_s][I_s] + \frac{d}{dt}[\Phi_s] \tag{3.30}$$

The same goes for the rotor voltages:

$$\begin{bmatrix} V_{ra} \\ V_{rb} \\ V_{rc} \end{bmatrix} = \begin{bmatrix} R_r & 0 & 0 \\ 0 & R_r & 0 \\ 0 & 0 & R_r \end{bmatrix} \begin{bmatrix} I_{ra} \\ I_{rb} \\ I_{rc} \end{bmatrix} + \frac{d}{dt} \begin{bmatrix} \Phi_{ra} \\ \Phi_{rb} \\ \Phi_{rc} \end{bmatrix} = \begin{bmatrix} 0 \\ 0 \\ 0 \end{bmatrix} \tag{3.31}$$

where:

$$[V_r] = [R_r][I_r] + \frac{d}{dt}[\Phi_r] = [0] \tag{3.32}$$

The rotor being short-circuited, its voltages are null.

- V_s: The matrix of phase voltages at the stator.
- V_r: The matrix of phase voltages at the rotor.
- I_s: The matrix of currents at the stator.
- I_r: The matrix of currents at the rotor.

3.3.0.4 Magnetic equations:

Each flux involves an interaction with the currents of all phases, including its own (notion of self-inductance):

$$\begin{bmatrix} \Phi_s \\ \Phi_r \end{bmatrix} = \begin{bmatrix} [L_s] & [M_{sr}] \\ [M_{rs}] & [L_r] \end{bmatrix} \begin{bmatrix} [I_s] \\ [I_r] \end{bmatrix} \tag{3.33}$$

Where:

$$[L_s] = \begin{bmatrix} L_s & M_s & M_s \\ M_s & L_s & M_s \\ M_s & M_s & L_s \end{bmatrix}$$

$[L_s]$ = Matrix of stator windings,
L_s = Self-inductance of a single stator winding,
M_s = Mutual inductance of coupling between stator windings.

$$[L_r] = \begin{bmatrix} L_r & M_r & M_r \\ M_r & L_r & M_r \\ M_r & M_r & L_r \end{bmatrix}$$

$[L_r]$ = Matrix of rotor windings,
L_r = Self-inductance of a single rotor winding,

M_r = Mutual inductance of coupling between rotor windings.

$$[M_{sr}] = [M_{rs}]^T = M_{sr} \begin{bmatrix} \cos\theta & \cos\left(\theta + \frac{2\pi}{3}\right) & \cos\left(\theta - \frac{2\pi}{3}\right) \\ \cos\left(\theta - \frac{2\pi}{3}\right) & \cos\theta & \cos\left(\theta + \frac{2\pi}{3}\right) \\ \cos\left(\theta + \frac{2\pi}{3}\right) & \cos\left(\theta - \frac{2\pi}{3}\right) & \cos\theta \end{bmatrix}$$

Where θ: The electrical angle defines the instantaneous relative position between the rotor axes and the stator axes, which are chosen as reference axes.

Finally, by substituting equation 3.33 into 3.30 and 3.32 we get the following:

$$[V_{sabc}] = [R_s][I_{sabc}] + \frac{d}{dt}\left([L_s][I_{sabc}] + [M_{sr}][I_{rabc}]\right) \tag{3.34}$$

$$[V_{rabc}] = [R_r][I_{rabc}] + \frac{d}{dt}\left([L_r][I_{rabc}] + [M_{rs}][I_{sabc}]\right) \tag{3.35}$$

3.3.0.5 Mechanical equation:

The study of the dynamic characteristics of asynchronous machines introduces variations not only in electrical parameters (voltage, current, EMF) but also in mechanical parameters (torque, speed). The equation of motion for the machine is written as:

$$T_{em} - T_L = J\frac{d\Omega}{dt} + f_r\Omega \tag{3.36}$$

Where:

- T_em: Electromagnetic torque of the machine. [Nm]
- T_L: torque of the mechanical load. [Nm]
- J: Moment of inertia. [Kg m^2]
- Ω: Angular velocity of the rotor, or the mechanical speed of the rotor.
- f_r: Friction coefficient [Nm / rad/s].

The electrical speed of the rotor:

$$\omega = p\Omega \tag{3.37}$$

Where p is the number of pole pairs. By substituting in equation 3.36 we get:

Thus:

$$T_{em} - T_L = \frac{J}{P}\frac{d\omega}{dt} + \frac{f}{P}\omega \tag{3.38}$$

3.3.0.6 Three-phase to two-phase transformation using PARK's transformation:

The condition for transitioning from a three-phase system to a two-phase system is the creation of a rotating electromagnetic field with equal magnetomotive forces.

The three-phase to two-phase transformation leads to a family of models of the asynchronous machine, where stator and rotor magnitudes are projected onto two quadrature axes. The idea behind this transformation is based on the fact that a balanced rotating field created by a three-phase system can equally be achieved by a two-phase system consisting of two coils offset by $\frac{\pi}{2}$ in space, and fed by currents phase-shifted by $\frac{\pi}{2}$ in time. The objective is to ensure that the magnetomotive forces and instantaneous power are conserved. For simplicity in our study, we first establish a model where the magnitudes are in a frame linked to the stator.

Thus, the winding equivalent to the three phases of the stator consists of two windings on the direct axes, α_s, and in quadrature, β_s. The direct axis α_s is aligned with the axis of the first phase a, static. Similarly, on the rotor, the two windings, α_s and β_s replace the equivalent three-phase windings.

Now, The Park transformation consists of a three-phase to two-phase transformation followed by a rotation. This transformation allows for moving from a three-phase frame (abc) to a two-phase orthogonal frame ($\alpha\beta$), and then to a rotating frame (dq). The $\alpha\beta$ frame remains fixed relative to the stator's abc frame, whereas the dq frame is mobile. It aligns with the $\alpha\beta$ frame by an angle referred to as the Park angle. This setup is essential for simplifying the control of AC motors by decoupling the flux and torque components. Figure 3.18 shows the park transformation vector diagram.

In the Park transformation, the reference frames for stator and rotor magnitudes must coincide to simplify their equations. This is achieved by linking the angles θ_s and θ_r as follows:

$$\theta_s = \theta + \theta_r$$

Hence, Park transformation can be applied to transforming voltages, currents, and fluxes as follows:

$$\begin{bmatrix} x_d \\ x_q \\ x_0 \end{bmatrix} = [P] \begin{bmatrix} x_a \\ x_b \\ x_c \end{bmatrix} \tag{3.39}$$

Where, The variable x represents voltage, current, or flux. The following indices are used for identification:

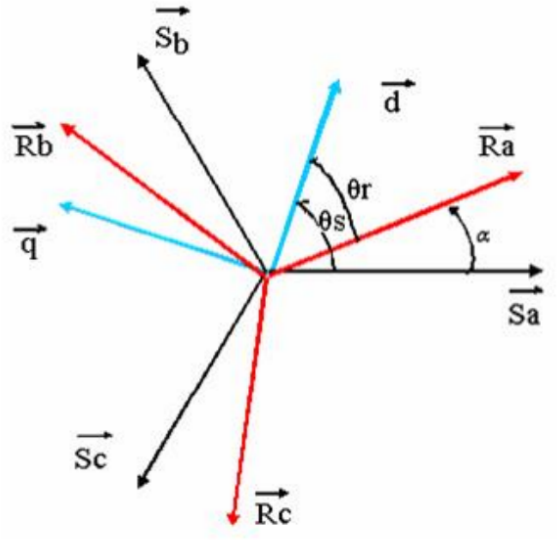

FIGURE 3.18: Representation of reference frames

- o: Index for the zero sequence axis.
- d: Index for the direct axis.
- q: Index for the quadrature axis.

Also, we have,

$$[P] = \sqrt{\frac{3}{2}} \begin{bmatrix} \cos\theta & \cos\left(\theta - \frac{2\pi}{3}\right) & \cos\left(\theta + \frac{2\pi}{3}\right) \\ -\sin\theta & -\sin\left(\theta - \frac{2\pi}{3}\right) & -\sin\left(\theta + \frac{2\pi}{3}\right) \\ \frac{1}{\sqrt{2}} & \frac{1}{\sqrt{2}} & \frac{1}{\sqrt{2}} \end{bmatrix} \tag{3.40}$$

where [P] is an orthogonal matrix; meaning that $[P(\theta)]^t = [P(\theta)]^{-1}$. This matrix is called the passing matrix and it is crucial for achieving Park's transformation. Its inverse is as follows:

$$[P(\theta)]^{-1} = \begin{bmatrix} \cos\theta & \sin\theta & \frac{1}{\sqrt{2}} \\ \cos\left(\theta - \frac{2\pi}{3}\right) & \sin\left(\theta - \frac{2\pi}{3}\right) & \frac{1}{\sqrt{2}} \\ \cos\left(\theta - \frac{4\pi}{3}\right) & \sin\left(\theta - \frac{4\pi}{3}\right) & \frac{1}{\sqrt{2}} \end{bmatrix} \tag{3.41}$$

Therefore, by considering the following:

$$[P]\left(\frac{d[P]^{-1}}{dt}\right) = \frac{d\theta}{dt}\begin{bmatrix}0 & -1 & 0\\ 1 & 0 & 0\\ 0 & 0 & 0\end{bmatrix} \tag{3.42}$$

We get for voltage in the dq axis:

$$\begin{aligned} V_{ds} &= R_s I_{ds} + \frac{d\phi_{ds}}{dt} - \frac{d\theta_s}{dt}\phi_{qs},\\ V_{qs} &= R_s I_{qs} + \frac{d\phi_{qs}}{dt} + \frac{d\theta_s}{dt}\phi_{ds},\\ V_{dr} &= R_r I_{dr} + \frac{d\phi_{dr}}{dt} - \frac{d\theta_r}{dt}\phi_{qr} = 0,\\ V_{qr} &= R_r I_{qr} + \frac{d\phi_{qr}}{dt} + \frac{d\theta_r}{dt}\phi_{dr} = 0. \end{aligned} \tag{3.43}$$

And since the angular speed in dq axis is equal to $\omega_s = \frac{d\theta_s}{dt}$, we get:

$$\begin{cases} V_{ds} = R_s I_{ds} + \frac{d\phi_{ds}}{dt} - \omega_s \phi_{qs},\\ V_{qs} = R_s I_{qs} + \frac{d\phi_{qs}}{dt} + \omega_s \phi_{ds},\\ R_r I_{dr} + \frac{d\phi_{dr}}{dt} - (\omega_s - \omega)\phi_{qr} = 0,\\ R_r I_{qr} + \frac{d\phi_{qr}}{dt} + (\omega_s - \omega)\phi_{dr} = 0. \end{cases} \tag{3.44}$$

Now, for the flux in dq axis we have:

$$\begin{cases} \Phi_{ds} = L_s I_{ds} + M I_{dr},\\ \Phi_{qs} = L_s I_{qs} + M I_{qr},\\ \Phi_{dr} = L_r I_{dr} + M I_{ds},\\ \Phi_{qr} = L_r I_{qr} + M I_{qs}. \end{cases}$$

The equations for torque and motion are given by:

$$T_{em} = pM(I_{qs}I_{dr} - I_{ds}I_{qr}) \tag{3.45}$$

Where:

$$\frac{J}{p}\frac{d\omega}{dt} = T_{em} - T_L - \frac{f}{p}\omega \tag{3.46}$$

- J: Moment of inertia of the rotor.
- f: Viscous friction coefficient.

- p: Number of pole pairs.
- T_em: Electromagnetic torque.
- T_L: torque of the mechanical load.

Until now, we have expressed the equations and quantities of the machine in a dq frame, which forms an electrical angle θ_s with the stator and also an electrical angle θ_r with the rotor, though it is not defined elsewhere, meaning it is free. Hence, there exist commonly three particular reference frames used in the modeling of the IM; model referred to the stator frame, the rotor frame, or the frame rotating at synchronous speed. In our case, we consider an induction motor model referred to the stator frame where the following assumptions for θ_s and θ_r are made:

$$\begin{aligned} \theta_s = 0, \quad & \theta_r = -\theta \\ \frac{d\theta_s}{dt} = 0, \quad & \frac{d\theta_r}{dt} = -\frac{d\theta}{dt} \\ \omega_s = 0, \quad & \omega_r = -\omega \end{aligned}$$

The electrical equations take the form:

$$\begin{cases} V_{ds} = R_s I_{ds} + \dfrac{d\phi_{ds}}{dt}, \\ V_{qs} = R_s I_{qs} + \dfrac{d\phi_{qs}}{dt}, \\ 0 = R_r I_{dr} + \dfrac{d\phi_{dr}}{dt} + \omega\phi_{qr}, \\ 0 = R_r I_{qr} + \dfrac{d\phi_{qr}}{dt} - \omega\phi_{dr}. \end{cases} \tag{3.47}$$

After rearranging the equations with $I_{ds}, I_{qs}, I_{dr}, I_{qr}$, we obtain:

$$\begin{cases} \dfrac{dI_{ds}}{dt} = -\dfrac{1}{T_s\sigma} I_{ds} + \dfrac{M^2}{L_s L_r \sigma}\omega I_{qs} + \dfrac{M}{L_s T_r \sigma} I_{dr} + \dfrac{M}{L_s\sigma}\omega I_{qr} + \dfrac{V_{ds}}{L_s\sigma}, \\ \dfrac{dI_{qs}}{dt} = -\dfrac{M^2}{L_s L_r \sigma}\omega I_{ds} - \dfrac{1}{T_s\sigma} I_{qs} - \dfrac{M}{L_s\sigma}\omega I_{dr} + \dfrac{M}{L_s T_r \sigma} I_{qr} + \dfrac{V_{qs}}{L_s\sigma}, \\ \dfrac{dI_{dr}}{dt} = \dfrac{M}{L_r T_s \sigma} I_{ds} - \dfrac{M}{L_r\sigma}\omega I_{qs} - \dfrac{1}{T_r\sigma} I_{dr} - \dfrac{\omega}{\sigma} I_{qr} - \dfrac{V_{ds} M}{L_s L_r \sigma}, \\ \dfrac{dI_{qr}}{dt} = \dfrac{M}{L_r\sigma}\omega I_{ds} + \dfrac{M}{L_r T_s \sigma} I_{qs} + \dfrac{\omega}{\sigma} I_{dr} - \dfrac{1}{T_r\sigma} I_{qr} - \dfrac{V_{qs} M}{L_s L_r \sigma}. \end{cases} \tag{3.48}$$

With:
$\sigma = 1 - \frac{M^2}{L_s L_r}$: The total leakage coefficient.
$T_s = \frac{L_s}{r_s}$: Stator time constant.
$T_r = \frac{L_r}{r_r}$: Rotor time constant.

The dq equivalent circuit of IM is shown in Figure 3.19 below:

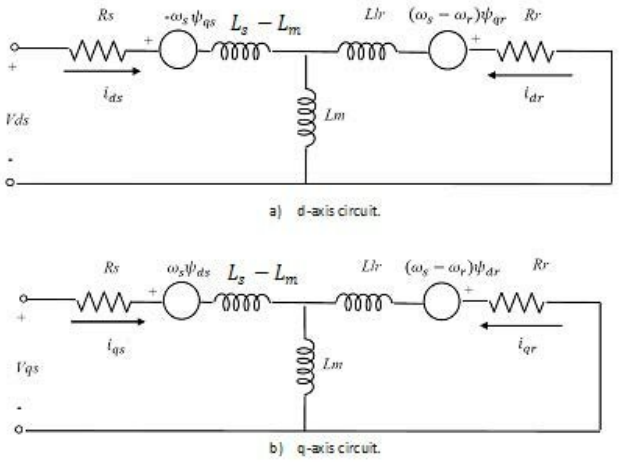

FIGURE 3.19: dq equivalent circuit of IM

These two circuits may be described in state space format as a linear time-invariant (LTI) system [Paper space], where we can write it as the following matrix form.

$$\frac{d}{dt}[\mathbf{x}] = [\mathbf{A}][\mathbf{x}] + [\mathbf{B}][\mathbf{V}]$$

Along with the closed-loop control system representing the matrix:

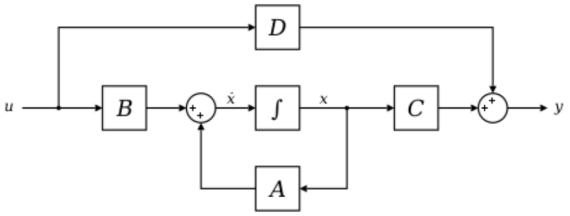

FIGURE 3.20: closed-loop control system representing the state space matrix

where,

[**A**]: The fundamental matrix that characterizes the system.

[**B**]: The input matrix.

[**C**]: The output matrix.

[**D**]: The direct transmission matrix.

[**X**]: The state vector.

We take for $[x]$:

$$[\mathbf{x}] = \begin{bmatrix} I_{ds} \\ I_{qs} \\ I_{dr} \\ I_{qr} \end{bmatrix}$$

Also, the matrix $[A]$ is set as follows:

$$[\mathbf{A}] = \begin{bmatrix} -\frac{1}{T_s\sigma} & (\omega_r + \frac{1}{\sigma}\omega) & \frac{M}{L_sT_r\sigma} & \frac{M}{L_s\sigma}\omega \\ (\omega_r + \frac{1}{\sigma}\omega) & -\frac{1}{T_s\sigma} & -\frac{M}{L_s\sigma}\omega & \frac{M}{L_sT_r\sigma} \\ \frac{M}{L_rT_s\sigma} & -\frac{M}{L_r\sigma}\omega & -\frac{1}{T_r\sigma} & (\omega_r - \frac{M^2}{L_sL_r\sigma}\omega) \\ \frac{M}{L_r\sigma}\omega & \frac{M}{L_rT_s\sigma} & (-\omega_r + \frac{M^2}{L_sL_r\sigma}\omega) & -\frac{1}{T_r\sigma} \end{bmatrix}$$

The matrix A could be split further into three sub-matrices A_1, A_2 and A_3 as shown:

$$[\mathbf{A}] = [\mathbf{A}_1] + \omega[\mathbf{A}_2] + \omega_r[\mathbf{A}_3]$$

Hence,

$$[A] = \begin{bmatrix} -\frac{1}{T_s\sigma} & 0 & \frac{M}{L_sT_r\sigma} & 0 \\ 0 & -\frac{1}{T_s\sigma} & 0 & \frac{M}{L_sT_r\sigma} \\ \frac{M}{L_rT_s\sigma} & 0 & -\frac{1}{T_r\sigma} & 0 \\ 0 & \frac{M}{L_rT_s\sigma} & 0 & -\frac{1}{T_r\sigma} \end{bmatrix} + \omega \begin{bmatrix} 0 & -1 & 0 & 0 \\ 1 & 0 & 0 & 0 \\ 0 & 0 & 0 & -1 \\ 0 & 0 & 1 & 0 \end{bmatrix} + \omega_r \begin{bmatrix} 0 & \frac{1}{\sigma} & 0 & \frac{M}{L_s\sigma} \\ -\frac{1}{\sigma} & 0 & -\frac{M}{L_s\sigma} & 0 \\ 0 & -\frac{M}{L_r\sigma} & 0 & -\frac{M^2}{L_sL_r\sigma} \\ \frac{M}{L_r\sigma} & 0 & \frac{M^2}{L_sL_r\sigma} & 0 \end{bmatrix}$$

Where,

$$[A_1] = \begin{bmatrix} -\frac{1}{T_s\sigma} & 0 & \frac{M}{L_sT_r\sigma} & 0 \\ 0 & -\frac{1}{T_s\sigma} & 0 & \frac{M}{L_sT_r\sigma} \\ \frac{M}{L_rT_s\sigma} & 0 & -\frac{1}{T_r\sigma} & 0 \\ 0 & \frac{M}{L_rT_s\sigma} & 0 & -\frac{1}{T_r\sigma} \end{bmatrix}$$

$$[\mathbf{A}_2] = \begin{bmatrix} 0 & 1 & 0 & 0 \\ -1 & 0 & 0 & 0 \\ 0 & 0 & 0 & 1 \\ 0 & 0 & -1 & 0 \end{bmatrix}$$

$$[\mathbf{A}_3] = \begin{bmatrix} 0 & \frac{1}{\sigma} & 0 & \frac{M}{L_s\sigma} \\ -\frac{1}{\sigma} & 0 & -\frac{M}{L_s\sigma} & 0 \\ 0 & -\frac{M}{L_r\sigma} & 0 & -\frac{M^2}{L_sL_r\sigma} \\ \frac{M}{L_r\sigma} & 0 & \frac{M^2}{L_sL_r\sigma} & 0 \end{bmatrix}$$

For [U] and [B] we have:

$$[U] = [V] = \begin{bmatrix} V_{ds} & V_{qs} & 0 \end{bmatrix}$$

$$[B] = \begin{bmatrix} \frac{1}{L_s\sigma} & 0 \\ 0 & \frac{1}{L_s\sigma} \\ -\frac{M}{L_sL_r\sigma} & 0 \\ 0 & -\frac{M}{L_sL_r\sigma} \end{bmatrix}$$

3.4 Pump Model:

Water pumps mainly fall into two categories based on the operating principle: dynamic pumps and positive displacement pumps, each of which has its own advantages and disadvantages depending on the application they are used in. A vast majority of irrigation pumps are centrifugal pumps which make part of the first category, and that is because of developing a high liquid velocity and pressure in diffusing flow passage, lower maintenance requirements, and cheaper which make them suitable for different irrigation applications. This particular solar pump uses an impeller (rotating part that transmits motion in a device) which spins the water rapidly in a casing, chamber, or housing. The spinning action is known as centrifugal force. This force is responsible for moving the water through the centrifugal pump. These solar centrifugal pumps may have several stages, in which the water passes through increasing pressure [44]. A centrifugal pump design is shown in Figure 3.21.

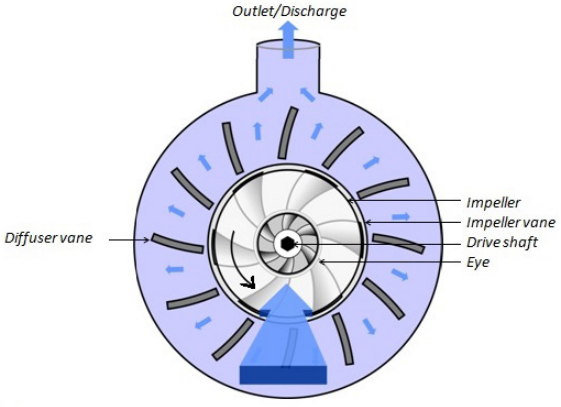

FIGURE 3.21: Centrifugal pump design

Each centrifugal pump applies a load torque proportional to the square of the rotor speed **??**.

$$T_L = K_p\Omega_r^2 \tag{3.49}$$

Where K_p is the proportionality constant and it is given by

$$K_p = \frac{P_{np}}{\Omega_{rn}^3} \tag{3.50}$$

The water rate and pressure of the pump depend on the available mechanical power at the rotating impeller and the total head. The determination of the pump's output parameters can be simplified using affinity laws [109, 111] which require only pump ratings and actual input parameters; rotor speed and torque.

$$\begin{cases} H' = \left(\frac{\Omega_r}{\Omega_{rn}}\right)^2 \cdot H \\ Q' = \left(\frac{\Omega_r}{\Omega_{rn}}\right) \cdot Q \\ P' = \left(\frac{\Omega_r}{\Omega_{rn}}\right)^3 \cdot P \end{cases} \tag{3.51}$$

Where H, Q and P are the rated parameters of the pump at speed Ω_{rn}, and H', Q' and P' are the parameters of pump at speed Ω_r different than the rated speed.

3.5 System design:

3.5.1 Design of PV array:

Our 2.2Kw motor-pump system is powered by a 3.19Kw PV array which consists of 10 modules in series. A PV module from AU Optronics PM300P00_315 with a peak voltage of 38.16V and a peak current of 8.36A is chosen. Both the power with respect to voltage (P-V) and the current versus voltage (I-V) curves characteristics of the PV model under STC are shown in Figure 3.22 along with all the PV specifications included within the table shown below.

3.5.2 Design of boost converter:

For the boost converter design, we start by finding the duty cycle for a DC bus voltage of 680V, as follows:

$$D = \frac{V_{dc} - V_{pv}}{V_{dc}} = \frac{680 - 381.6}{680} = 0.44 \tag{3.52}$$

$$L = \frac{D \times V_{pv}}{f_{sw} \times I_{mp}} = \frac{0.44 \times 381.6}{10000 \times (8.36 \times 0.2)} \approx 10.2\,\text{mH} \tag{3.53}$$

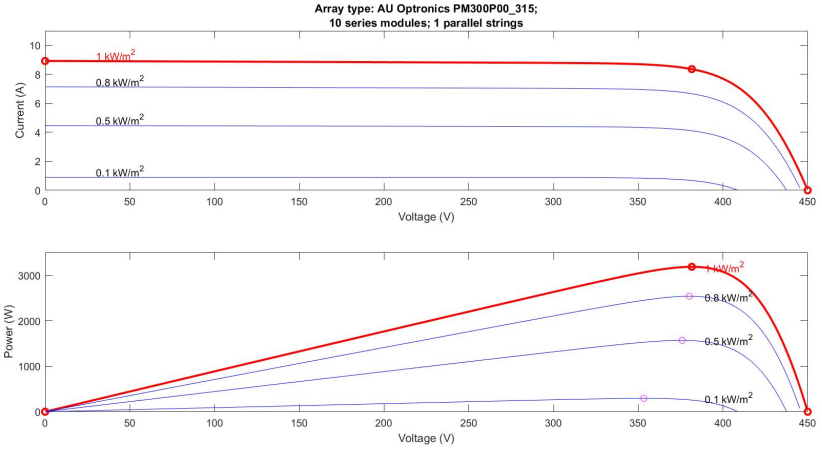

FIGURE 3.22: P-V and I-V characteristics for **AU Optronics PM300P00_315** PV module

TABLE 3.2: AU Optronics PM300P00_315 Module Data

Parameter	**Value**
Module	AU Optronics PM300P00_315
Maximum Power (W)	319.0176
Open circuit voltage V_{oc} (V)	45
Voltage at maximum power point V_{mp} (V)	38.16
Temperature coefficient of V_{oc} (%/deg.C)	-0.33151
Cells per module (Ncell)	72
Short-circuit current I_{sc} (A)	8.92
Current at maximum power point I_{mp} (A)	8.36
Temperature coefficient of I_{sc} (%/deg.C)	0.062601

Where:

$V_{dc} = 680\,\text{V}$ is the dc-bus voltage of the VSI.

$f_{sw} = 10000\,\text{Hz}$ is the switching frequency of the boost converter.

I_L is the ripple in the current through L, $I_L = I_{mp}$.

$$C = \frac{I_{dc}}{2\omega_L \cdot \Delta V_{dc}} = \frac{\frac{3190}{680}}{\cdot 2 \cdot (2\pi \cdot 50) \cdot (680 \cdot 0.053)} \approx 207\,\mu F \tag{3.54}$$

Where:

I_{dc}: is an average current flowing through the dc-bus.

ω: is the line frequency in rad/s.

ΔV_{dc}: is the ripple in the dc-bus voltage.

3.5.3 Design of motor-pump system:

The following parameters shown in table 3.3 are chosen for our motor-pump system based on the requirements of our stand-alone SWPS.

TABLE 3.3: Pump-motor parameters

Parameter	**Value**
Power	2.2 (kW)
Speed	1480 (rpm)
TDH	81.4 (m)
Q	4.2 (m^3/hr)
Rs	0.4125 (ω)
LS	0.0154 (H)
Msr	0.2845 (H)
Rr	2.486 (ω)
Lr	0.018 (H)
J	0.0132 (Kg.m^2)
Fr	0.00219 (N.m.s)
P	2

3.6 Conclusion:

At the end of this chapter, one could have a general idea of all the different components this Stand-alone SWPS consists of. Starting by giving a brief explanation of how solar cells work along with modeling the PV generator. Then, power converters were discussed through exploring their power circuits and characteristics. Moreover, a complete explanation of the IM model along with all the necessary transformations was done. In addition to a general description of the centrifugal pump showing its efficiency, torque equation, and the affinity laws that allow the estimation of changes in pump performance due to changes in shaft speed. Finally, we covered the design of the overall system by choosing the appropriate PV generator suitable for our motor pump system, boost converter, and the common DC-link capacitor.

Chapter 4

Simulation of the stand-alone SWPS

Introduction

In this chapter, A complete explanation on how the proposed stand-alone solar water pumping system's SIMULINK model was implemented to test and verify its different functionalities under various operating conditions. This chapter starts first by covering the control strategies used in our system mainly the DTC and the different MPPTs used in controlling both the DC boost converter and the IM. The stand-alone SWPS will be simulated using SIMULINK and based on the results different discussions will be made to clarify the well-behaving of our system.

4.1 Control Strategies

Here in this section we will cover the control strategies incorporated within our stand-alone SWPS. Starting with the Maximum Power Point Tracking (MPPT) which is crucial for optimizing the energy harvested from the solar panels. It ensures that the solar panels operate at their most efficient point, which is the maximum power point (MPP), under varying metrological conditions. By doing so, MPPT maximizes the use of available solar energy, enhancing the overall efficiency of the solar pumping system. This is especially beneficial in applications where it is essential to maximize the water volume pumped while using solar energy efficiently, such as in remote or off-grid locations where traditional power sources are unavailable or unreliable. For this system, two types of MPPT were used: classic p&o and a proposed p&o.

For the speed control of IM using VSI, the direct torque control technique (DTC) is used to drive the IM, focusing on controlling the amount of current needed to generate a certain torque. Figure 4.1 below illustrates the different control blocks used within our system.

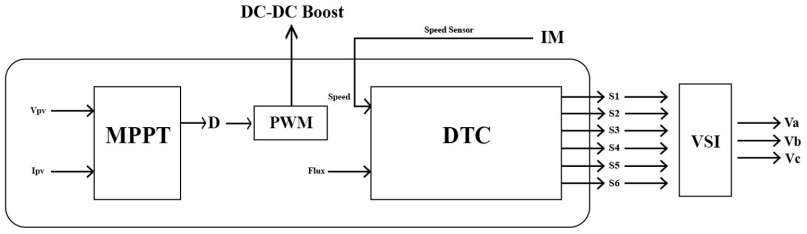

FIGURE 4.1: Control system components

4.1.1 Direct Torque Control:

Direct Torque Control (DTC) was introduced by Takahashi in 1986. Unlike vector Control, this technique doesn't need Park transformation, PI regulators, and any speed or position sensors which make it easy to implement with IMs. The principle of DTC is to control the electromagnetic torque of the motor independently of the flux and that is by adjusting the torque angle while keeping the magnitude of the stator flux constant, the rotor then will be almost constant over a wide variation of torque **?**. as shown in equation 4.1 below.

$$T_e = \frac{3}{2}\frac{P}{2}\frac{L_m}{\delta L_s L_r}\psi_s \psi_r \sin(\theta_T) \tag{4.1}$$

where,

$$\sigma = 1 - \frac{L_m^2}{L_s L_r} \tag{4.2}$$

ψ_s, ψ_r are known as the rated magnitudes of stator flux and rotor flux $\tilde{\psi}_s, \tilde{\psi}_r$, respectively. Whereas θ_T is the angle between the two flux vectors, called also Torque angle.

The basic functional blocks used to implement the DTC scheme are represented in figure 4.2. The instantaneous values of the stator flux and torque are calculated from the stator

variable by using a closed-loop estimator. Stator flux and torque can be controlled directly and independently by properly selecting the inverter switching configuration [14].

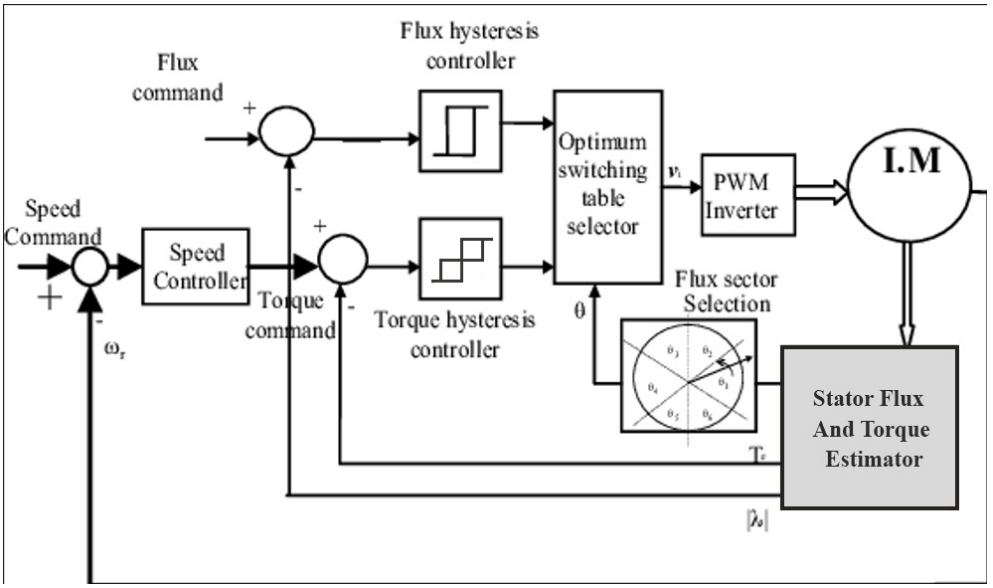

FIGURE 4.2: Basic DTC scheme for IM drives

As seen above, the DTC block diagram has a flux sector selector block that is used based on the following set of equations. First recalling from equation 3.28 in Chapter 3 we get:

$$\vec{v}_s = R_s\vec{i}_s + \frac{d\vec{\psi}_s}{dt} \implies \vec{\psi}_s(t) = \vec{\psi}_s(t-\Delta T) + \int_{t-\Delta T}^{t}\left(\vec{v}_s - R_s\vec{i}_s\right)dt \tag{4.3}$$

The equation above shows that the stator flux changes instantly in response to the variations in stator voltage, which is an output of the PWM inverter and regulated via space vector modulation. During this brief interval, the stator current, typically dependent on load fluctuations, remains constant. Thus, we have:

$$\psi_s(t) = \psi_s(t-\Delta T) + \vec{V}_s\Delta T \Rightarrow \Delta\psi_s = \vec{V}_s\Delta T \tag{4.4}$$

If we consider ΔT as a sampling interval of $[0, T_s]$, during which the switching states of the inverter are constant, and since T_s is constant, then equation 4.4 becomes:

$$\Delta\psi_s = \vec{V}_s T_s \tag{4.5}$$

Thus, the stator flux position is divided into six distinct sectors, each spanning 60 degrees as shown in figure 4.3 below.

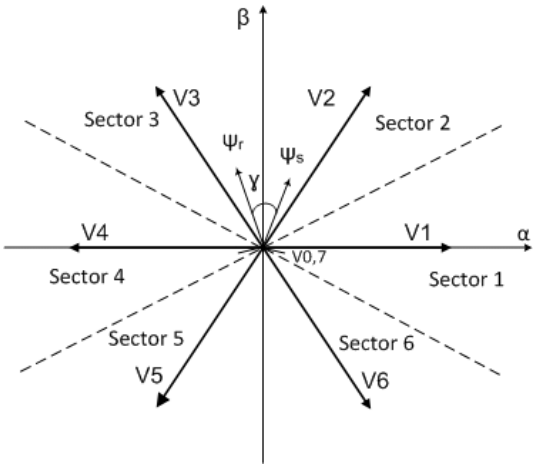

FIGURE 4.3: Active vectors of stator voltages and corresponding sectors

as a result, the variations of the stator flux and torque angle are controlled independently by selecting the appropriate stator voltage vector based on the look up table illustrated below.

TABLE 4.1: Classical DTC switching table

Comparator output		**Sector**					
x_ψ	x_T	1	2	3	4	5	6
+1	+1	$\vec{V}_2$	$\vec{V}_3$	$\vec{V}_4$	$\vec{V}_5$	$\vec{V}_6$	$\vec{V}_1$
	0	$\vec{V}_7$	$\vec{V}_0$	$\vec{V}_7$	$\vec{V}_0$	$\vec{V}_7$	$\vec{V}_0$
	-1	$\vec{V}_6$	$\vec{V}_1$	$\vec{V}_2$	$\vec{V}_3$	$\vec{V}_4$	$\vec{V}_5$
-1	+1	$\vec{V}_3$	$\vec{V}_4$	$\vec{V}_5$	$\vec{V}_6$	$\vec{V}_1$	$\vec{V}_2$
	0	$\vec{V}_0$	$\vec{V}_7$	$\vec{V}_0$	$\vec{V}_7$	$\vec{V}_0$	$\vec{V}_7$
	-1	$\vec{V}_5$	$\vec{V}_6$	$\vec{V}_1$	$\vec{V}_2$	$\vec{V}_3$	$\vec{V}_4$

Therefore, based on the result of the hysteresis comparator, a certain sector is selected which may affect both torque and flux either by increasing or decreasing.

4.1.2 The speed selector

In this section the algorithm used for selecting the reference speed is explained through the use of the following equations. The load torque is relevant to speed as shown in equation 4.6 below.

$$T_L = K\omega^2 \tag{4.6}$$

Where,

T_l: Is the load torque in N/m,

K: Load gain,

ω: Speed in rad/s

And it is known that power is written as follows:

$$P = T_L \omega \tag{4.7}$$

Substituting 4.6 in 4.7 we get:

$$P = K\omega^3 \tag{4.8}$$

For the rated power we also have:

$$P_{\text{rated}} = K\omega_{\text{rated}}^3 \tag{4.9}$$

Dividing 4.7 on 4.9 we get:

$$\frac{P}{P_{\text{rated}}} = \left(\frac{\omega}{\omega_{\text{rated}}}\right)^3 \tag{4.10}$$

Solving for ω we get:

$$\omega = \omega_{\text{rated}} \sqrt[3]{\frac{P}{P_{\text{rated}}}} \tag{4.11}$$

Equation 4.11 produces the reference speed, which subsequently serves as an input for the direct torque control (DTC) algorithm to facilitate torque generation.

4.1.3 Maximum power point tracker:

Even though PV panels seem to be good electricity generators, their efficiency is relatively low, with conversion efficiency typically in the range of 12 up to 20%. This range of efficiency can drop to some lower values during different irradiances, temperatures, and load conditions **?**. Hence, PV systems need to operate around the maximum power point, or as near to it as possible for maximum efficiency, therefore, the use of electronic maximum power point tracker (MPPT) systems is employed. A typical MPPT system consists of a switch mode power converter inserted between the PV source and the load, for the duty ratio of the converter an algorithm controls it to enable continuous tracking of the MPP **?**. In **?** many MPPTs were developed with variations in the degree of simplicity, sensor requirement, cost, tracking speed, the hardware used for implementation, popularity, and many other aspects.

Many Maximum power point tracking algorithms were proposed in the literature. Some methods are based on perturbation such as the Perturb and Observe (P&O), hill climbing (HC), and Incremental Conductance (IC) MPPT techniques **??**, **??**. Though simple and cost-effective, many times they lead to oscillations around the MPP, which results in energy waste. Hence, other techniques were developed to reduce the power losses caused by dynamic tracking errors under rapid weather-changing conditions such as Constant Voltage Control (CVC) applied in **?**, The fuzzy logic controllers also have been introduced in the tracking of

the MPP in PV systems **?**, and ANN-based MPPT, which once been well-fitted to the training data, exhibits superior dynamic performance in comparison to PO and InCond MPPTs.

Even though Many algorithms were suggested in the literature to cope with P&O issues, it is still one of the commonly used techniques nowadays due to its ease of implementation in a low-cost controller, and it has relatively good MPP tracking performance when compared to the other techniques **?**. This is why working on enhancing the P&O algorithm is a better choice, that is what has been proposed in our thesis through the use of a new P&O technique that retains the same characteristics of a classical P&O but additionally, it tracks much faster and has fewer oscillations around the MPP which contributes positively to the overall conversion efficiency of the PV system. The next sections will discuss the comparison between these two MPPTs under different climate conditions.

4.1.3.1 Perturb and Observe MPPT:

Solar PV array has nonlinear bell-shaped P_{PV} versus V_{PV} characteristics as shown in previous Chapters above. At any moment, the operating point depends on the impedance of the load connected to the array terminals. A maximum power point tracker (MPPT) then is used to track the point of operation on the PV curve. There have been many algorithms proposed in the literature used for tracking the maximum power point in PV systems, the most basic one of all is the perturb and observe algorithm (P&O). The P&O algorithm is one of the most commonly used methods in practice, it operates by periodically perturbing, i.e. incrementing or decrementing, the array terminal voltage and comparing the PV output power with that of the previous perturbation cycle. If the PV array operating voltage changes and power increases, the control system moves the PV array operating point in that direction. Otherwise, the operating point is moved in the opposite direction, figure 4.4 demonstrates the principle of the P&O algorithm **?**.

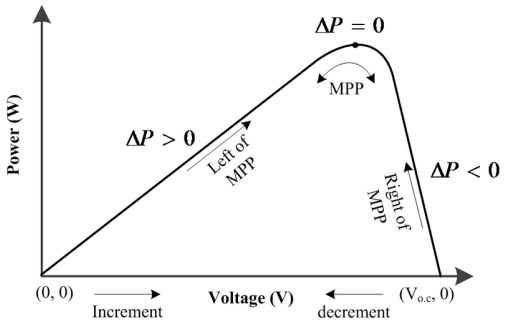

FIGURE 4.4: Conventional P&O MPPT algorithm

The DC-DC controller adjusts slightly the voltage from the PV array and measures power, then it varies the terminal voltage of the PV and takes a second measurement of the power, if the difference between the current power measurement and the previous one is positive, hence, voltage is incremented in that same direction, otherwise, we decrement till reaching the maximum power point where the difference in power is zero $\Delta P = 0$. Figure 4.5 shows the flowchart of the P&O technique.

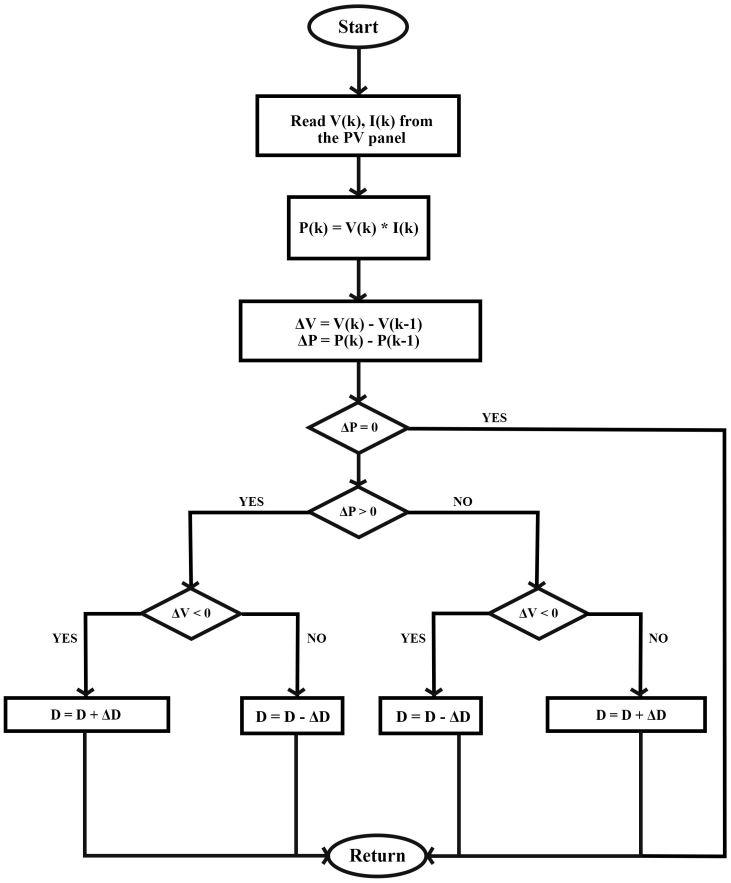

FIGURE 4.5: Flowchart of P&O MPPT algorithm

4.1.4 Stand-alone SWPS performance using classical P&O algorithm:

In this section, a comprehensive performance analysis of the system is conducted using the classical Perturb and Observe (P&O) algorithm, with evaluation based on several parameters including output photovoltaic (PV) power, voltage, current, as well as motor speed, torque, and flow rate all that will be under different irradiance levels.

Our Perturb and Observe (P&O) technique is implemented using Simulink blocks, chosen for their simplicity and the algorithm's efficiency in run mode. This approach is favored over coding with M-files, which occasionally present challenges in interfacing with the Simulink model.

This algorithm generates duty cycles and interacts with the Boost converter through the use of a PWM as shown in Figure 4.6 below.

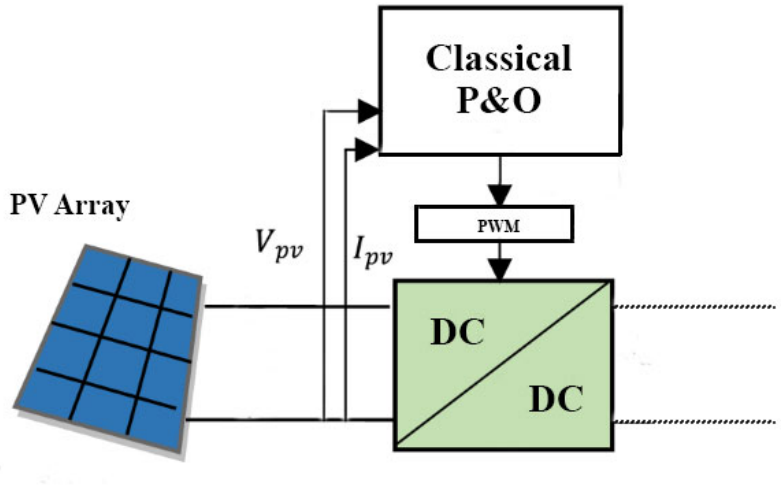

FIGURE 4.6: Block diagram of classical P&O MPPT with the direct control

4.1.4.1 Fixed irradiance condition:

For this section, our system is operating under the STC (1000 w/m^2), using the classical P&O algorithm. The results are illustrated in Figures from 4.7 to 4.12 shown below.

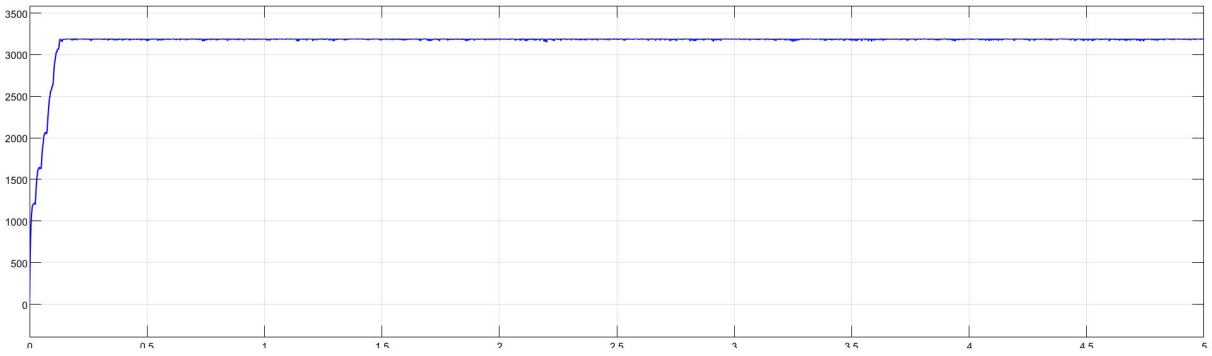

FIGURE 4.7: PV output power under fixed irradiance condition

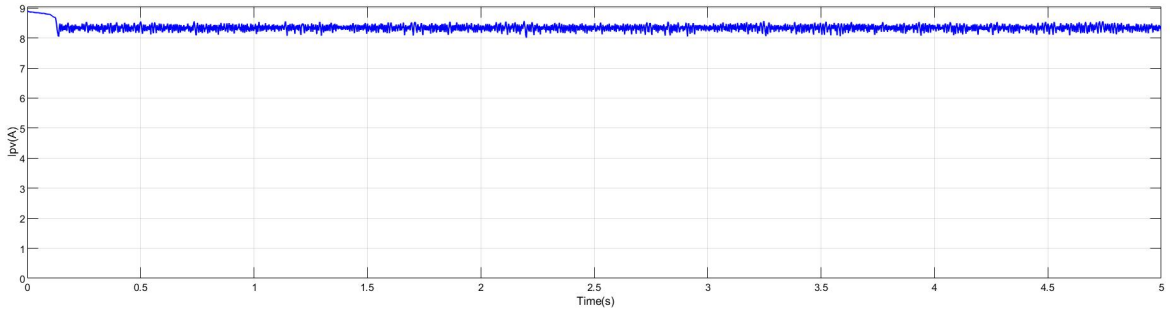

FIGURE 4.8: PV output current under fixed irradiance condition

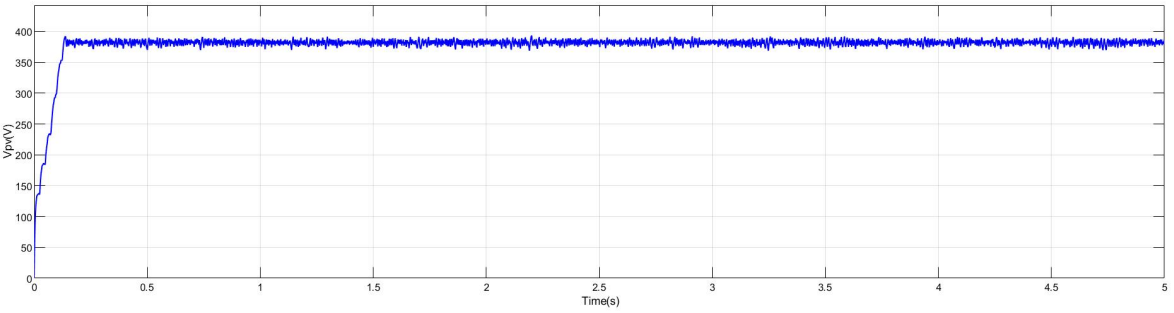

FIGURE 4.9: PV output voltage under fixed irradiance condition

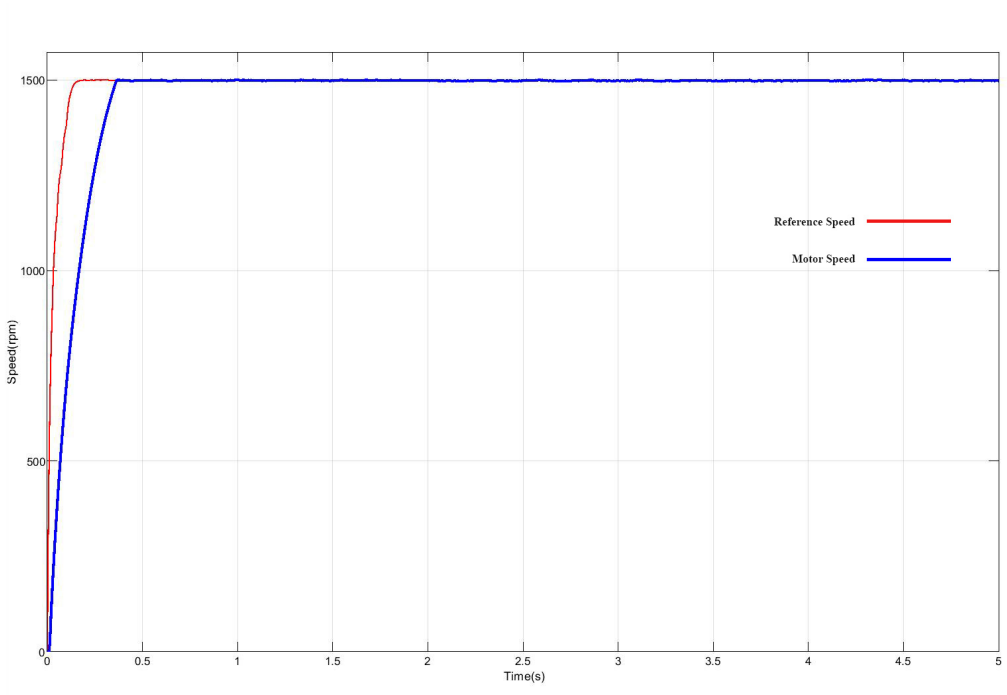

FIGURE 4.10: IM speed under fixed irradiance condition

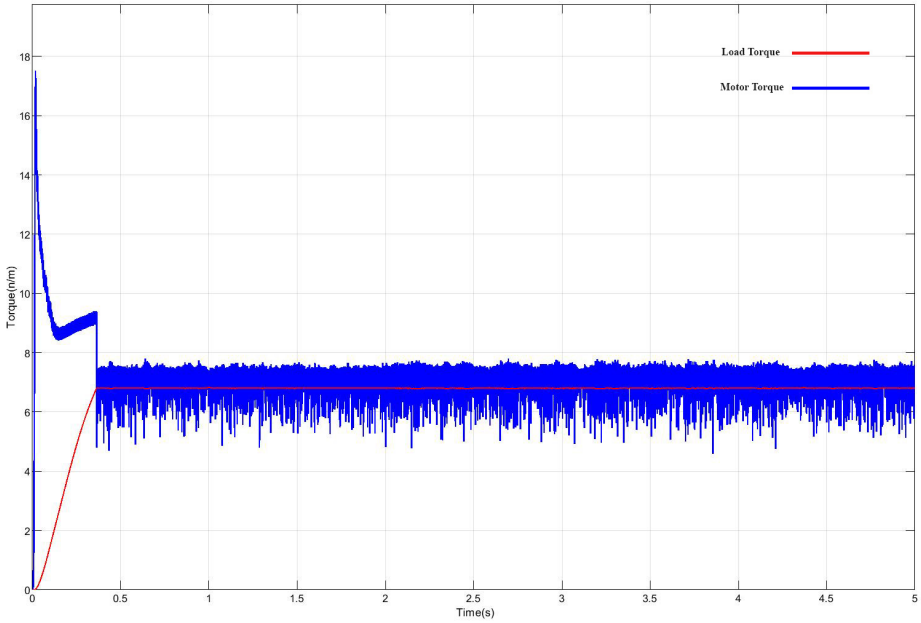

FIGURE 4.11: IM torque under fixed irradiance condition

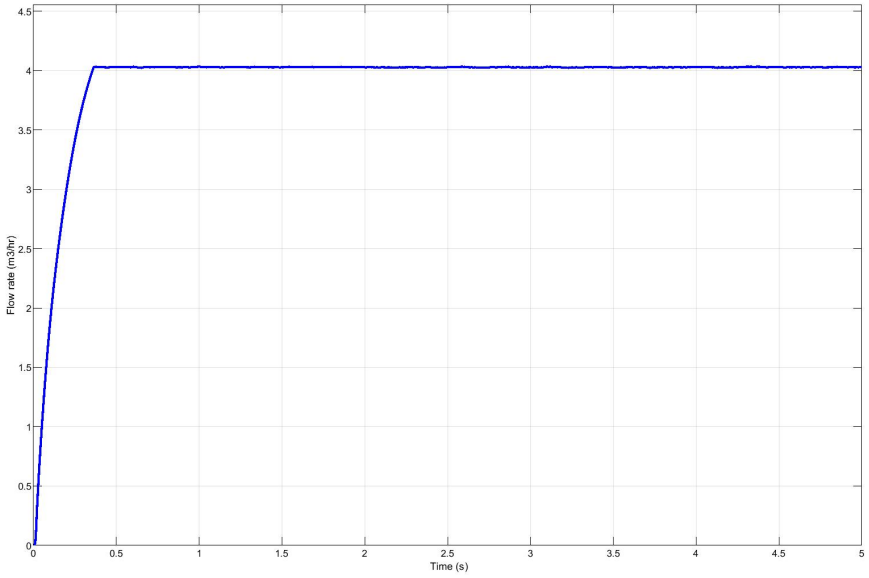

FIGURE 4.12: Pump flow rate under fixed irradiance condition

We notice from the curve shown above, that the classical P&O algorithm even under fixed irradiance results in high oscillations around the MPP, which converts to energy less, as a

result, the PV efficiency will drop due to this phenomenon. Moreover, the tracking time is a bit slow, which in the case of fast irradiance changes may cause a loss track of MPP.

4.1.4.2 Variable irradiance condition:

To test for the system's stability and tracking response, we need to operate under variable irradiances also, which is a common case in real-world setups. Figure below shows 4.13 different irradiance levels used for our Simulink model.

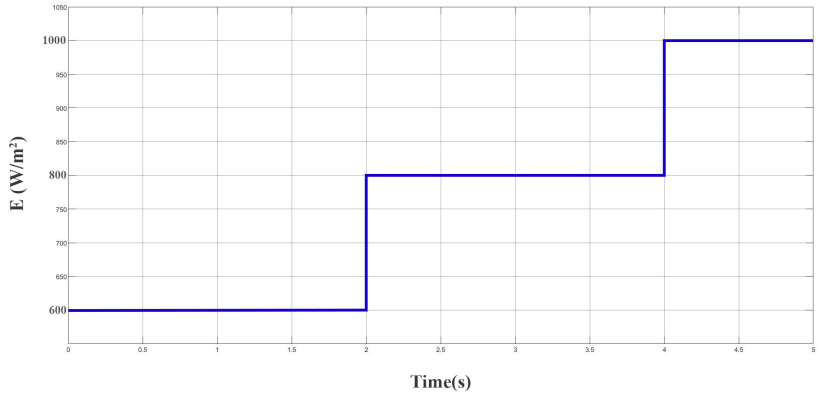

FIGURE 4.13: Irradiance levels used for our Simulink model

Hence, we get the following results shown below.

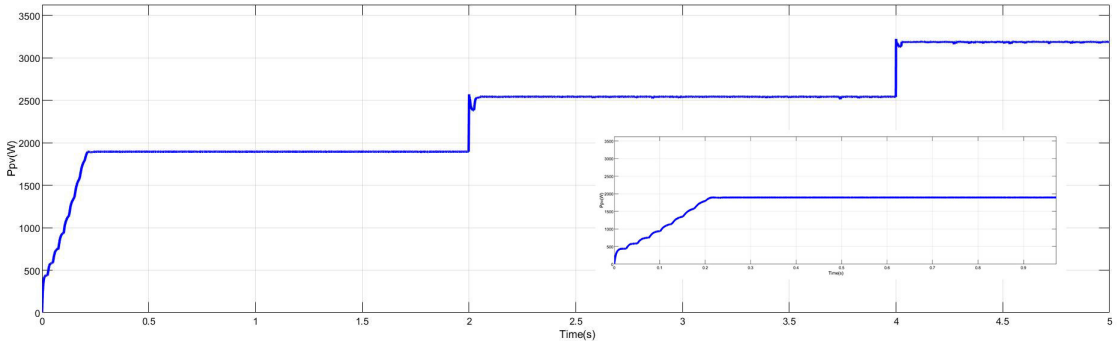

FIGURE 4.14: PV output power under different irradiance conditions

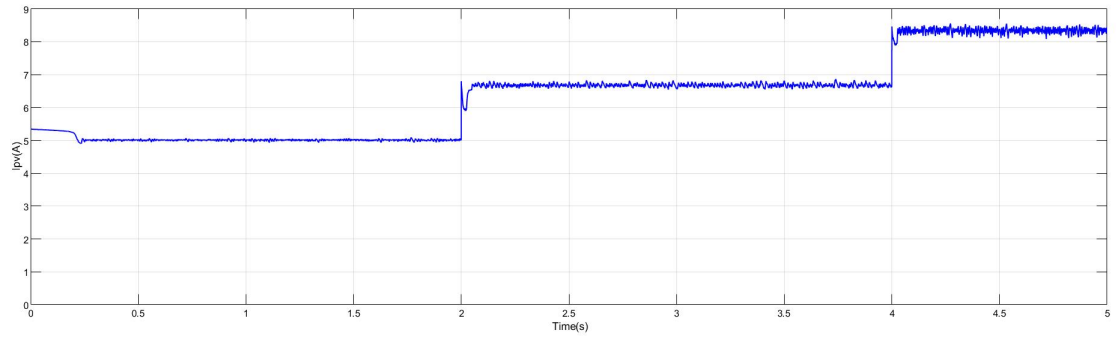

FIGURE 4.15: PV output current under different irradiance conditions

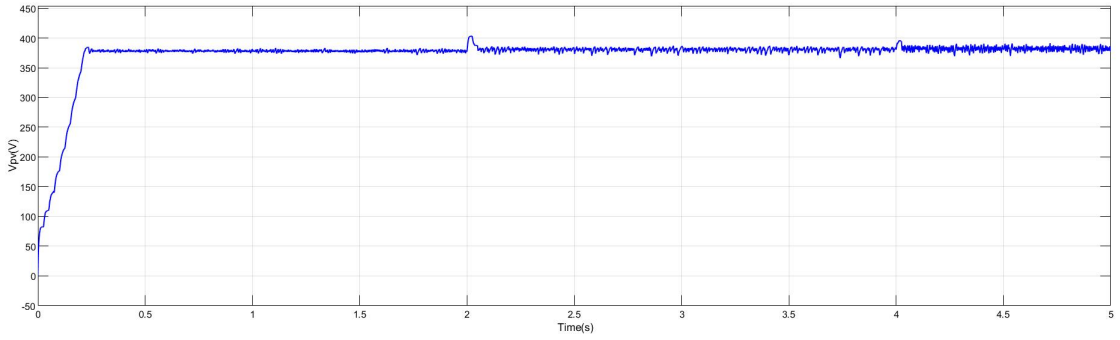

FIGURE 4.16: PV output voltage under different irradiance conditions

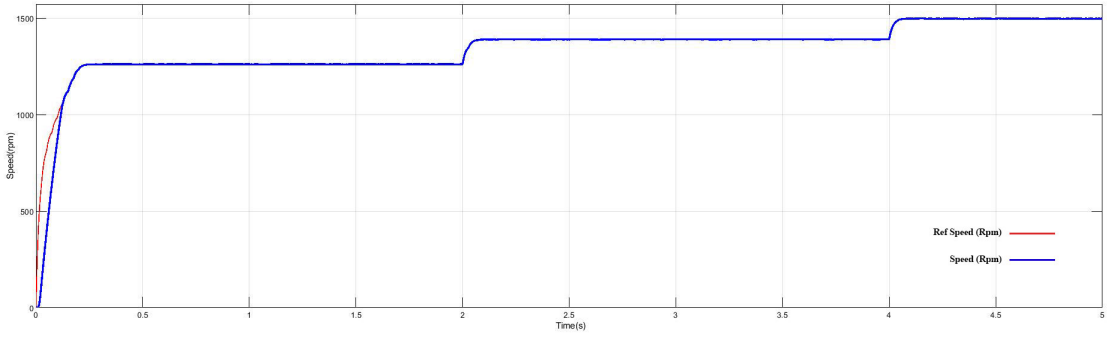

FIGURE 4.17: IM speed under different irradiance conditions

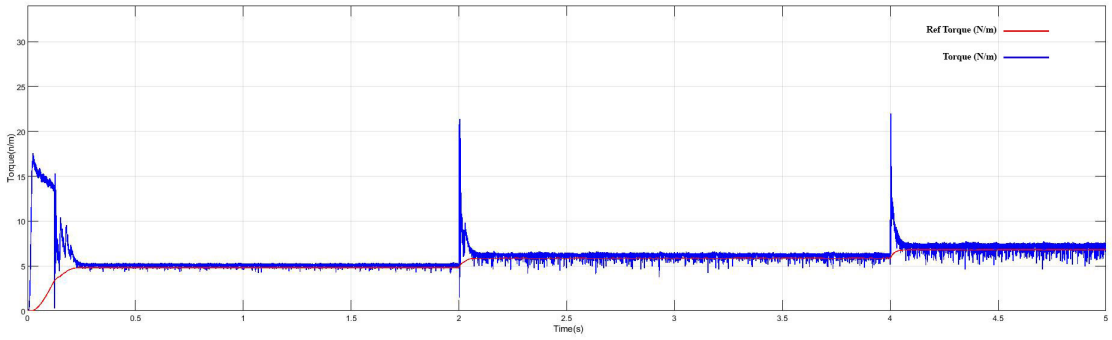

FIGURE 4.18: IM torque under different irradiance conditions

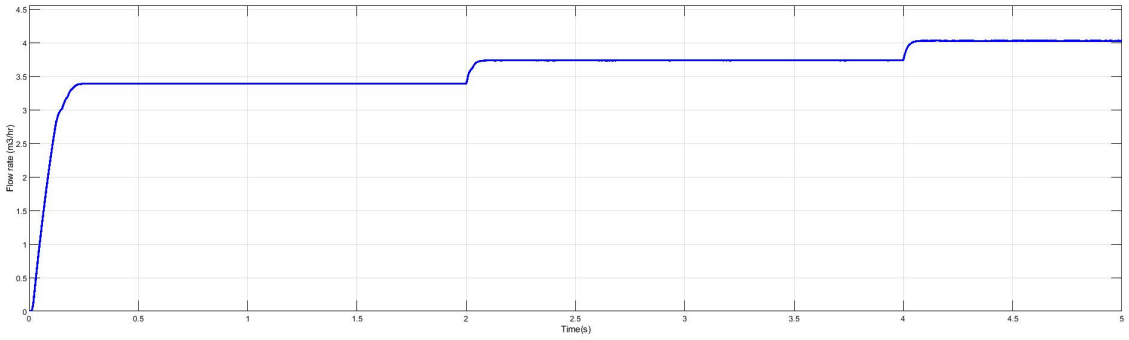

FIGURE 4.19: Pump flow rate under different irradiance conditions

Figures from 4.14 to 4.19 show how under different irradiance conditions the system behaves differently, such that at an irradiance of 600 w/m^2 power delivered by the PV is at 1.9kw, and this value will keep increasing till reaching the rated power 3.19kw for 1000 w/m^2. This affects in return the motor-pump system's operation, as seen in Figure 4.19 the flow rate starts approximately at 3.4 m^3/hr at 600 w/m^2 and starts increasing until reaching the rated flow rate at 1000 w/m^2. The same patterns of variation are observed with both torque and speed, indicating that this system exhibits changes in operational parameters in response to fluctuating irradiance levels. Such variability mirrors real-world conditions to which our stand-alone Solar Water Pumping System (SWPS) would be subjected over a day, across diverse meteorological environments. Table 4.2 below illustrates the numerical results obtained under different irradiance levels for MPP from PV and MPP from the classical P&O algorithm.

TABLE 4.2: Performance parameters of the PV system at different irradiance levels

Irradiance (W/m^2)	MPP from PV array (W)	MPP (W)
1000	3190	3189
800	2543	2540
600	1895	1894

4.1.4.3 Variable temperature condition

Now, a variable temperature condition is applied on our PV array following the pattern shown in Figure 4.20, results are illustrated in Figures below.

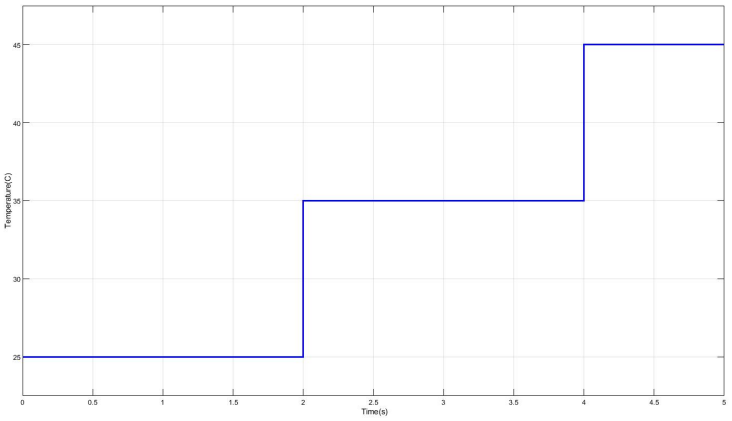

FIGURE 4.20: Temprature levels used for our Simulink model

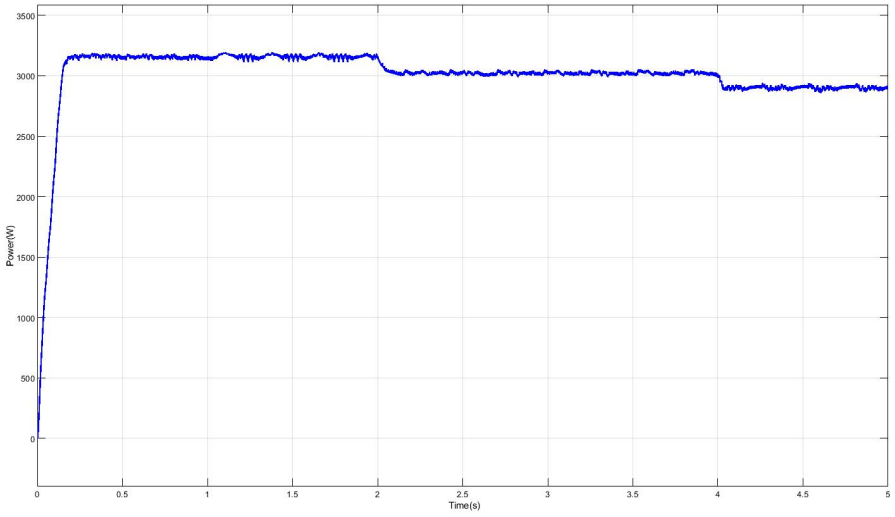

FIGURE 4.21: PV output power under variable temprature conditions using classical P&O

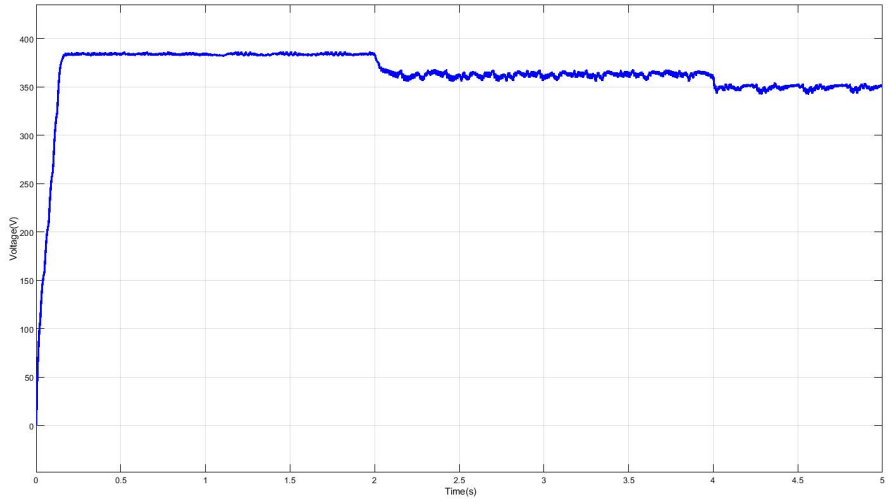

FIGURE 4.22: PV output voltage under variable temprature conditions using proposed P&O